Biophysical *Journal*
Article

Biophysical Society

A Mechanism for Cytoplasmic Streaming: Kinesin-Driven Alignment of Microtubules and Fast Fluid Flows

Corey E. Monteith,[1] Matthew E. Brunner,[2] Inna Djagaeva,[1] Anthony M. Bielecki,[1] Joshua M. Deutsch,[2,*] and William M. Saxton[1,*]

[1]Department of Molecular Cell and Developmental Biology and [2]Department of Physics, University of California Santa Cruz, Santa Cruz, California

ABSTRACT The transport of cytoplasmic components can be profoundly affected by hydrodynamics. Cytoplasmic streaming in *Drosophila* oocytes offers a striking example. Forces on fluid from kinesin-1 are initially directed by a disordered meshwork of microtubules, generating minor slow cytoplasmic flows. Subsequently, to mix incoming nurse cell cytoplasm with ooplasm, a subcortical layer of microtubules forms parallel arrays that support long-range, fast flows. To analyze the streaming mechanism, we combined observations of microtubule and organelle motions with detailed mathematical modeling. In the fast state, microtubules tethered to the cortex form a thin subcortical layer and undergo correlated sinusoidal bending. Organelles moving in flows along the arrays show velocities that are slow near the cortex and fast on the inward side of the subcortical microtubule layer. Starting with fundamental physical principles suggested by qualitative hypotheses, and with published values for microtubule stiffness, kinesin velocity, and cytoplasmic viscosity, we developed a quantitative coupled hydrodynamic model for streaming. The fully detailed mathematical model and its simulations identify key variables that can shift the system between disordered (slow) and ordered (fast) states. Measurements of array curvature, wave period, and the effects of diminished kinesin velocity on flow rates, as well as prior observations on f-actin perturbation, support the model. This establishes a concrete mechanistic framework for the ooplasmic streaming process. The self-organizing fast phase is a result of viscous drag on kinesin-driven cargoes that mediates equal and opposite forces on cytoplasmic fluid and on microtubules whose minus ends are tethered to the cortex. Fluid moves toward plus ends and microtubules are forced backward toward their minus ends, resulting in buckling. Under certain conditions, the buckling microtubules self-organize into parallel bending arrays, guiding varying directions for fast plus-end directed fluid flows that facilitate mixing in a low Reynolds number regime.

INTRODUCTION

Transport processes that purposefully move organelles, chromosomes, and other objects from one place to another through cytoplasm are fundamental to the reproduction, growth, and development of eukaryotic cells. To drive transport, dimeric molecular motors couple alternating cycles of ATP-driven conformation change to cycles of filament binding and release to generate stepping forces that move motor-attached cargoes along cytoskeletal filaments (1). In many cases, the primary purpose of motor activity is to deliver individual cargoes to specific destinations. However, in other processes, the objective is to transfer force from motors to their filament tracks and/or to the cytoplasmic fluid that surrounds them. We report here a mathematical model for the mechanism of a microtubule-motor-driven process whose purpose is to drive fluid motion in a manner that accomplishes the mixing of two different masses of viscous cytoplasm. The process, cytoplasmic streaming in *Drosophila* oocytes, offers unique insights into how the responses of fluid and filament tracks to forces that are generated by motors can have long-range influences on cytoplasmic motion and organization. Our results provide a concrete quantitative framework for understanding the hydrodynamic underpinnings of transport processes, elucidate a general and hitherto unknown form of filament self-organization, and point out an intriguing mechanism for mixing fluids at low Reynolds number.

In the *Drosophila* ovary, a germline stem cell generates an egg chamber with 15 nurse cells that are connected by

Submitted February 1, 2016, and accepted for publication March 21, 2016.

*Correspondence: josh@ucsc.edu or bsaxton@ucsc.edu

Corey E. Monteith and Matthew E. Brunner contributed equally to this work.

William M. Saxton and Joshua M. Deutsch contributed equally to this work.

Editor: David Sept.

http://dx.doi.org/10.1016/j.bpj.2016.03.036

cytoplasmic channels to one another and to the anterior end of a developing oocyte. During the early and middle stages of oogenesis, mRNAs, protein complexes, and organelles synthesized in nurse cells are selectively transported into the oocyte (2). Disordered cytoplasmic flows ("slow streaming") help disperse the new components after they enter the oocyte anterior. During this period, developmental determinants such as bicoid and oskar mRNA particles are transported toward particular regions of the oocyte margin and anchored to the cortex, thereby establishing the major body axes of the future organism (3–6). Meanwhile, substantial amounts of material synthesized in somatic tissues, such as yolk, are transferred into the developing oocyte through follicle cells along its lateral membranes by endocytosis. In late oogenesis, at the beginning of stage 10B, nurse cells squeeze all their remaining cytoplasm into the oocyte anterior en masse. To mix this new material with the existing yolky ooplasm, cytoplasmic flows accelerate >10-fold and become coherent, following long, varying trajectories throughout the oocyte ("fast streaming") (7). Mutations that allow premature fast streaming and its associated mixing prevent the localization of developmental determinants to their cortical target areas and thus disrupt the proper formation of body-axis polarity (8). Mutations that allow no fast streaming prevent the mixing of the oocyte with nurse-cell cytoplasm and can also cause embryonic lethality (9–11). Therefore, the biophysical mechanism that underlies fast streaming is important.

The force for streaming is generated by a plus-end-directed microtubule motor, kinesin-1 (10). In mid-oogenesis, before stage 10B, microtubules, many of which are nucleated at the oocyte cortex where γ-tubulin-based nucleation complexes are concentrated, extend their plus ends inward, forming a dynamic 3-D meshwork (11–13). Kinesin-1 is abundant and diffusely distributed (10,14). The trajectories of slow cytoplasmic flows, as seen by observing the movements of yolk endosomes or other organelles, are short and randomly directed. At stage 10B, flows become fast, long-range, and ordered as a layer of subcortical microtubules organizes into parallel bending arrays (11,13). This transition from slow to fast streaming coincides with a dispersal of cortical γ-tubulin and the loss of a diffuse f-actin meshwork that permeates the ooplasm (15,16). It is particularly interesting that depolymerization of that f-actin meshwork, which should decrease cytoplasmic viscosity, allows premature fast streaming as early as stage 9 (8,15).

From these and other observations, qualitative models have proposed that the normal slow-streaming process during mid-oogenesis reflects plus-end-directed kinesin-1 transport of cargoes that act as impellers to transfer force to cytoplasm that generates disordered fluid flows. Although the oocyte is capable of organizing subcortical microtubules into parallel arrays and driving fast, ordered flows, the process is restrained until stage 10B by certain factors, especially the cytoplasmic f-actin network (8,10,11,15,16). Weakening of that network at stage 10B allows a self-amplifying loop of kinesin-1-driven fast plus-end-directed fluid motion along with increasing microtubule alignment that helps generate long-range flows. In combination, these observations suggest that fast streaming is a self-organizing process with a relatively simple mechanism comprised of four principal components: a stationary cortical barrier, a population of microtubules whose minus ends are tethered to that barrier, kinesin-1 motor complexes, and cytoplasmic fluid.

To elucidate the streaming mechanism, we combined experimental observations with detailed mathematical modeling based on fundamental physical principles. Fluorescence microscopy of live oocytes examined relationships between the oocyte cortex, subcortical green-fluorescent-protein (GFP)-microtubule behavior, and streaming-driven motions of organelles. Based on those observations and the previous qualitative streaming hypotheses, a concrete quantitative model was developed using established estimates for microtubule stiffness, kinesin-1 velocity on microtubules, and cytoplasmic viscosity. The model defines size/spacing relationships for various kinesin cargoes that could generate enough viscous drag to drive the fast-streaming velocities that were observed. We then focused on a simple analysis of the effects of equal-opposite kinesin forces on the behavior of a single microtubule whose minus end is tethered in an imposed cytoplasmic flow field. Starting from any random configuration, kinesin forces along the length of the microtubule generate bending patterns that evolve into a stable helical wave that can become sinusoidal when adjacent to a nonmoving cortex-like barrier plane. To examine a more complex situation similar to that in an oocyte, we coupled the models for kinesin-driven cytoplasmic flow generation and filament bending to determine the behavior of a field of many microtubules with minus ends held stationary near a barrier plane in a self-generated flow field. Simulations show that microtubule behaviors evolve into the two states that are seen in oocytes; either noncorrelated helical bending, akin to slow streaming, or remarkably correlated parallel arrays that bend in a sinusoidal manner parallel to the cortical plane, akin to fast streaming. Key factors that determine evolution of the noncorrelated or correlated state are spacing between the cortex-like barrier and the level at which microtubules can become parallel to it, microtubule stiffness, and parameters that determine kinesin-derived force density along the microtubules: motor-cargo size/spacing, motor velocity, and cytoplasmic viscosity. The facts that the two simulation outcomes are analogous to the two states seen in oocytes and that they emerge over a full range of parameter variations suggest that the model is valid and that it provides a robust quantitative mechanism for kinesin-mediated cytoplasmic streaming.

MATERIALS AND METHODS

Theoretical modeling and simulations

The central work here develops theoretical analyses and computer simulations of the mechanism of cytoplasmic streaming in *Drosophila* oocytes. Fully detailed mathematical analyses are presented in the Supporting Material. Three major parts to the modeling approach will be presented in Results.

- Analysis of hydrodynamic flow induced by kinesin motion along microtubules. We employ theoretical calculations and numerical work to predict the magnitude of flow fields.
- Waves created on a microtubule by kinesin motion. We develop and analyze a continuous model for this problem, leading to a detailed understanding of the steady-state nonlinear waves that are generated. Computer simulations are also employed to obtain quantitative estimates of frequency and wavelength based on parameters such as microtubule stiffness and ooplasmic viscosity.
- Full hydrodynamic treatment of many microtubules and kinesin. We develop and implement a numerical model to describe this more complex situation, in which kinesin motors on different microtubules interact hydrodynamically, generating complex collective behavior. This leads to the investigation of a nonequilibrium disorder-order transition that takes place as model parameters are varied.

Genetics

To observe fluorescent microtubules in oocytes, a single copy of transgenic *UASp-GFPS65c-α-tub84B* was expressed in the female germline using *P{w$^+$ GAL4::VP16nos.UTR}MVD1* (nanos-Gal4) as a driver. To obtain egg chambers that were additionally homozygous for slow-*Khc* mutations, germline clones were induced in the GFP-tubulin background using an FLP/FRT mitotic recombination approach in females heterozygous for either *Khc*^{23} or *Khc*^{17}, as described previously (11). Egg chambers with a half dose of wild-type kinesin were obtained from females that were heterozygous for a small deletion that removes the *Khc* gene (*Df(2R)BSC309/+*). To observe lipid droplet motions, GFP-LD (*P{UASp-GFP-LD}*), which fuses the lipid-droplet-binding domain of Klar-β to GFP, was expressed in the female germline using the nanos-GAL4 driver (17).

Microscopy

Egg chambers were dissected from adult females and were mounted live in halocarbon oil on coverslips as described previously (11). They were imaged in time lapse with either a spinning-disk confocal fluorescence microscope (Fig. 1; Movies S1, S2, and S3) or an Olympus FV1000 two-photon fluorescence microscope (see Fig. 7; Movie S8). Fluorescence redistribution after photobleaching (FRAP) tests were performed using the Olympus FV1000 "bleach laser" function set to a wavelength of 880 nm at maximum intensity for a duration of 0.24 s.

Organelle and microtubule motions

Curve radii for microtubule arrays were measured from time-lapse images of GFP-tubulin in fast-streaming oocytes. For clearly visible array waves, the radius was determined by fitting the most acute wave apex with a circle. Wave periods for arrays that remained visible in the optical section for sufficient duration were estimated from time-lapse videos by determining the time required for a complete wave cycle (peak to peak or front to front) to pass a fixed position. FRAP patterns were determined by plotting the average pixel intensity of a 15-μm-long line translated sideways along a 24 μm path following the long axis of the bleached rectangles.

To analyze streaming motions of organelles, three approaches were used. First, in spinning-disk images of oocytes that expressed GFP tubulin, organelles appeared dark by virtue of excluding the GFP. For each oocyte, the positions of the centers of 10 randomly selected dark organelles that were beneath the immobile oocyte cortical zone and that remained in the plane of focus for at least 50 s were marked in each frame using an MTrackJ version 1.5.0 plug-in for ImageJ version 1.42 (18). Velocity was determined by measuring the net distance traveled between the start and end points and dividing by time. This simple low-frequency sampling approach filtered out the influence of short-range multidirectional saltatory motions, thus focusing velocity values on bulk cytoplasmic flow (11). The second approach focused on yolk endosomes in egg chambers lacking GFP-tubulin. The abdomens of females were injected with 1 mg/mL trypan blue dye, which is coendocytosed with yolk from hemolymph by oocytes (11). After 2–4 h, ovaries were dissected and imaged using red fluorescent protein filters. Fluorescent endosomes were tracked and velocities were determined as for the GFP-tubulin-excluding organelles. In the third approach, females that expressed GFP-LD, which is targeted to lipid droplets, were injected with trypan blue and ovaries were imaged in two colors using GFP filters for GFP-LD and red fluorescent protein filters for trypan blue. To measure streaming velocities, three different areas within each of five oocytes were selected, in which endosomes and lipid droplets were free of the cortex and moved in the focal plane. In the center of each area, a line was drawn that followed the path of motion using ImageJ. A kymograph was then constructed (ImageJ, Velocity Measurement Tool Macro) that revealed pixel intensity changes along that line as a function of time. In each GFP-LD kymograph, slopes were measured for five randomly selected, well-defined GFP streaks and then averaged to reflect lipid-droplet velocity in that area. The three kymographs were then averaged to produce a velocity value for each oocyte.

RESULTS

Streaming flows and microtubule bending

To gain insight into the behaviors of microtubules and cytoplasm during streaming, we used time-lapse fluorescence microscopy to image live oocytes dissected from female *Drosophila* that expressed GFP-tubulin in their germlines (Fig. 1; Movies S1 and S2). Comparison of stage 9 (slow-streaming) and stage 10B (fast-streaming) oocytes revealed striking differences. Fibrous fluorescence from microtubules in stage 9 was disordered. Motions of GFP-excluding organelles were also disordered and accomplished little net displacement over time (Fig. 1, A and B; Movie S1). The microtubule and organelle patterns did not vary substantially at different depths beneath the oocyte surface. In stage 10B, near the oocyte margin, microtubule fluorescence was dispersed among a layer of large organelles (~5 μm in diameter) that moved little, presumably constrained by association with the cortex (Fig. 1, C and D, *lower left*). At ~5 μm beneath that cortical layer and parallel to the plasma membrane, there was a dense zone of aligned microtubules that exhibited correlated wave-like bending behaviors. Organelles just inward from that microtubule layer moved fast over long distances, generally following the paths of the adjacent microtubule arrays. The average velocity determined by tracking of randomly selected GFP-excluding organelles, including slow ones associated with the cortex, was 217 $\pm$ 38 nm/s (n = 12 oocytes). To examine the streaming behaviors of specific organelles, females expressing GFP-LD, which tags lipid droplets that enter the oocyte

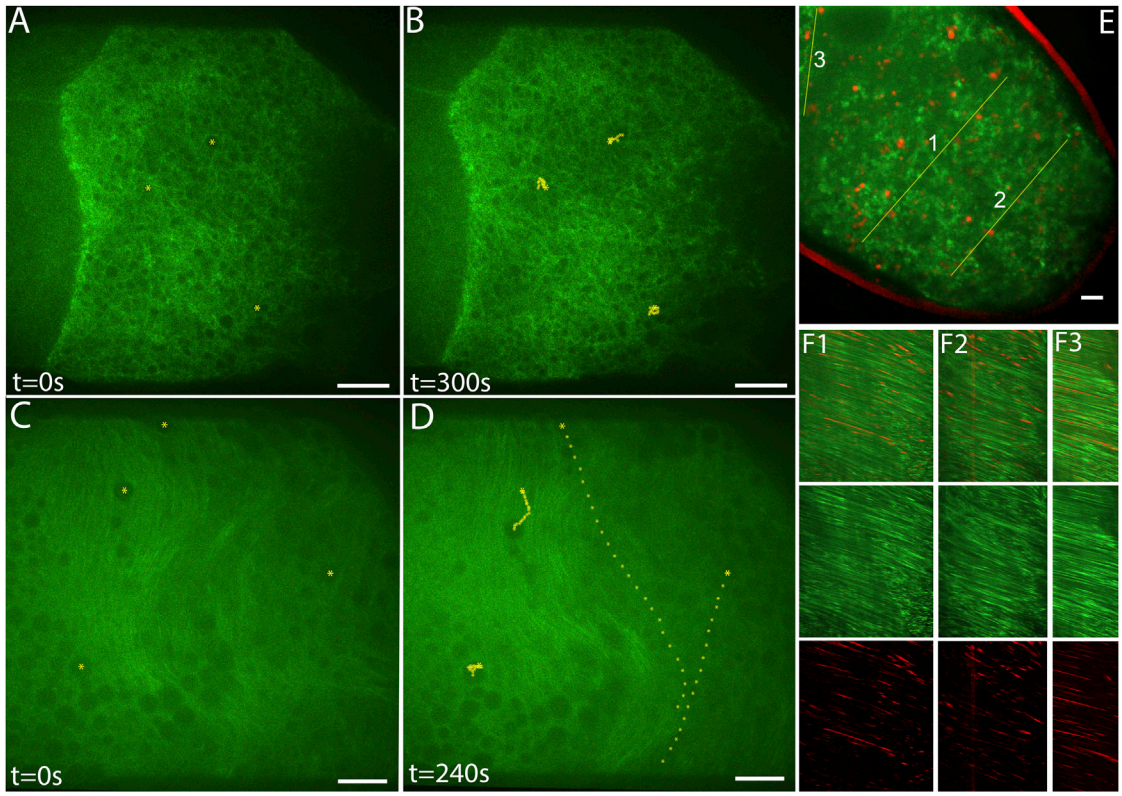

FIGURE 1 Microtubule organization and organelle motion in *Drosophila* oocytes. (*A–D*) Single optical sections from beneath the plasma membranes of live oocytes that contained GFP-α-tubulin (see other examples in Movies S1 and S2). (*A*) A stage 9 oocyte in which the centers of three yolk granules are marked with yellow dots. (*B*) The same oocyte 5 min later, with the positions of the three yolk granules marked at intervening 10 s intervals. The optical section is near the surface of the oocyte at the right side and is ~10 μm deeper at the left side. Note at all depths the similarly disordered microtubules and slow granule movements. (*C* and *D*) A stage 10B oocyte with granules marked and tracked as in (*A*) and (*B*). In this case, the optical section is just beneath the oocyte surface at the lower left and is ~10 μm deeper on the right. Note the parallel microtubule arrays at ~5 μm depth. Organelle motion was negligible between the microtubule layer and the oocyte surface (*left side*), and was fast beneath the microtubule layer (*right side*). Only yolk endosomes that remained in the focal plane were used to mark streaming motions in this figure. (*E*) A single optical section from a time-lapse image series (Movie S3) showing a stage 10B oocyte with lipid droplets marked by GFP-LD (*green*) and endosomes carrying trypan blue (*red*). The yellow lines were used for generating the kymographs in (*F*). (*F*) Kymographs show the intensities of lipid-droplet and endosome signals along the lines marked in (*E*) (*x* axes) over time (*y* axis = 800 s). Scale bars, 10 μm.

anterior from nurse cells, were injected with trypan blue, which is taken up by the oocyte during endocytosis of yolk through lateral surfaces. Two-color time-lapse images (Fig. 1, E and F; Movie S3) showed that endosomes were relatively immobile in and near the cortex, but moved fast beneath it. Lipid droplets were excluded from the cortex and moved fast beneath it. The patterns of motion and the velocities of lipid droplets and endosomes that were free of the cortex were the same, reflecting bulk cytoplasmic flows. The average velocity of GFP-tagged lipid droplets determined from kymographs of oocyte regions that had relatively linear flow patterns (Fig. 1 *F*) was 313 $\pm$ 27 nm/s (mean $\pm$ SE of $n = 5$ oocytes).

A mechanism for kinesin-driven fluid flow and microtubule bending

Our findings, joined with past work described in the Introduction, support a self-organizing motility mechanism that is unique in its simplicity, relying primarily on a single filament type, microtubules, and a single motor protein species, kinesin-1. At the beginning of stage 10B, changes occur that allow robust movement of kinesin-1 along microtubules whose minus ends are thought to be tethered to the cortex. The kinesin-1 motors and their associated cargoes transfer force to adjacent cytoplasmic fluid by viscous drag, and hence, cytoplasm moves toward the plus ends. The force of each kinesin-1 on fluid is matched by an equal and opposite force on the microtubule that would displace it with the minus end leading, if it were free to move. However, because its minus end is tethered to the cortex, the microtubule responds to the kinesin force by buckling. In the fast-streaming state, hydrodynamic force transfer between neighboring microtubules, combined with drag on them from bulk cytoplasmic flow toward their plus ends, encourages parallel alignment and a correlation of bending behaviors. The correlated bending patterns vary over time, creating varying trajectories for fluid flows that facilitate

nonlaminar motions and thus promote efficient mixing of cytoplasm, despite its high viscosity and the small scale.

Fluid flow caused by kinesin-driven motion

To elucidate the intuitive mechanism in quantitative terms, we considered three lines of inquiry. 1) How can bulk cytoplasmic fluid flows be driven by the movement of kinesin motors toward microtubule plus-ends? 2) How does microtubule bending occur in this situation? 3) How can the combination of these two effects lead to a self-organizing system of fast flows, aligned microtubules, and correlated bending behavior? To address these questions, a mathematical model was developed based on the physical principles of hydrodynamics. Simulations of the model with various parameters unexpectedly led to either disordered or aligned phases that resemble the slow- and fast-streaming states observed in oocytes.

To begin, we developed a physical model for fluid flows based on known properties of microtubules, kinesin-1, and cytoplasm. A small moving object will interact with its surrounding cytoplasm by viscous drag (19,20), moving the fluid such that flow velocity decreases with distance away from the object, r, as $1/r$. Thus, a single kinesin-cargo complex traveling along a microtubule can move neighboring fluid, but the velocity of that movement becomes negligible at large distances. However, consider an in-vivo-like situation with many kinesin-cargoes traveling along a microtubule. As illustrated in Fig. 2, a linear array of spherical objects of diameter a, moving at velocity v_0, that are separated by distances d, will create drag similar to that of a long rod. As analyzed in detail in Section S2 in the Supporting Material, for distance scales $\gg d$, this train of objects is equivalent to a solid rod of diameter a, moving at a velocity of $\sim(a/d)v_0$. Because of its long length, a moving rod can generate a flow field with velocities that are substantial at large distances. In fact, the effect of a moving rod of length L is similar to the effect of a moving sphere of diameter L, up to slowly varying logarithmic corrections (19). Thus, fluid velocity will be comparable to that of the rod out to distances of order L. With kinesin-cargo complexes closely spaced all along a microtubule, L will be equivalent to the length of the microtubule, which in an oocyte could average tens of microns.

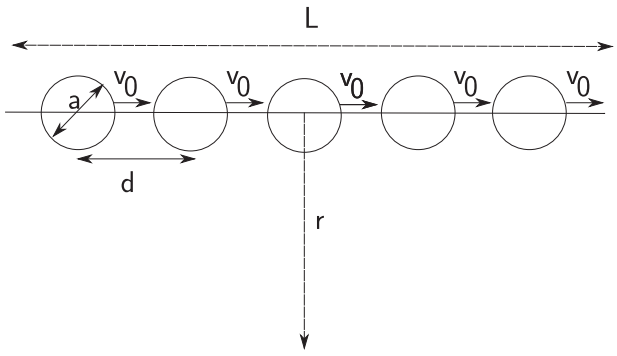

FIGURE 2 Fluid movement by viscous drag on a train of motor-cargo complexes. A train of spherically shaped impellers of diameter a and separation d, all moving in a fluid with low Reynolds number at velocity v_0. The fluid velocity, $v(r)$, is measured at a point distance r from the axis. Separated by small distances, the moving spheres should behave as a rod of length L.

This analysis neglects the effect of the oocyte cortex, which will inhibit fluid flow next to its surface, since it is stationary. To analyze this cortical effect on a flow field generated by many aligned microtubules, similar to the situation during fast streaming, we considered an infinite array of parallel rods lying above a wall (Fig. 3). To simplify, instead of kinesin complexes moving along the rod surfaces, each rod (*red*) is modeled as moving along its length, which causes equivalent viscous drag and thus hydrodynamic flow. The cortex-like barrier below it imposes a fluid velocity of zero (*dark blue*) at its surface. The hydrodynamics of this situation can be understood by electrostatic analogy, because it maps onto the problem of an array of rods at constant potential above a grounded plane and can be solved by the method of images. In this case, fluid far from the wall and the array of rods moves at a constant intermediate velocity (Fig. 3, *green*). Therefore, a largely two-dimensional layer of microtubules near the cortex with closely spaced kinesin cargoes moving along them could cause mass fluid flow in an oocyte.

Now we are in a position to determine the relationship between the velocity of kinesin and that of ooplasm during fast streaming. The velocity of ooplasm should be less than that of kinesin moving along cortical microtubules by a factor of $\sim a/d$. Kinesin-1-driven motions in metazoan cells vary from ~100 to 1000 nm/s depending on which cargo type is being tracked, probably on regulatory influences, and perhaps also on how many kinesins are engaged in moving each cargo (21–24). We elected to use the velocity of kinesin-1 itself measured directly in cells at $v_0 = 780$ nm/s (25). In our tests, the average velocity of fast-streaming lipid droplets beneath the microtubule layer is 313 ± 27 nm/s, suggesting that a/d is 0.4. With an average cargo diameter of $a = 250$ nm (e.g., lipid droplets), a spacing of $d = 625$ nm along microtubules should be sufficient to support the observed mass fluid velocity. Electron microscopy showing close association between lipid droplets and subcortical microtubules in stage 10B oocytes led originally to the suggestion that they are key streaming impellers (13). However, any kinesin-cargo complex should suffice if it is appropriately spaced along microtubules; e.g., filamentous kinesin cargoes such as microtubules with an average length of 5 μm would need to be spaced at only 3.13 μm and 40-nm-diameter small vesicles would need to be spaced closely at 100 nm. This logic leads to consideration of the possibility that kinesin-1 motors, each with its own rod-like geometry 30–80 nm long (26), could drive fast streaming if they were active without cargo bound and if they were closely spaced along microtubules.

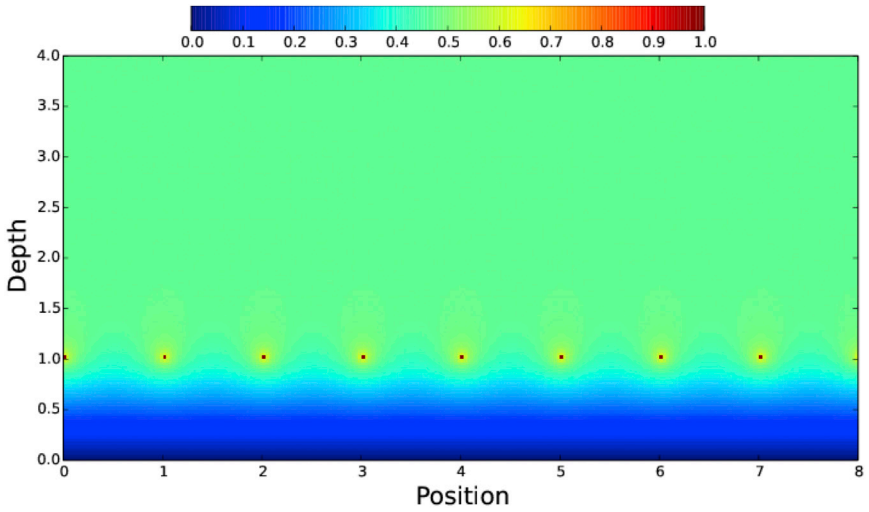

FIGURE 3 Model of a fluid flow velocity field generated by kinesin-like motion. Shown is a cross-sectional view of an array of infinitely long microtubule-like rods (*red dots*) suspended in fluid at a depth of 1 (arbitrary units) above a nonmoving cortex-like barrier ($y = 0$). Coated evenly with kinesin-cargo complexes moving at a constant velocity into or out of the page, each rod generates fluid flow in that same direction. Relative fluid velocities are represented by colors as shown above in the color bar, with red being equivalent to the kinesin velocity, yellow and green to intermediate velocity, and blue to slow velocity. Velocity is fastest around each microtubule, goes linearly to zero at the cortical barrier plane, and asymptotes to a constant intermediate value (*green*) above.

In summary, this fluid-flow analysis indicates that kinesin forces that are transferred to cytoplasmic fluid by viscous drag on any sort of cargo can indeed explain the magnitude and velocity of fluid motion in fast-streaming oocytes, even at substantial distances from the subcortical microtubule layer.

Dynamics of kinesin-driven microtubule bending

Can kinesin forces explain the correlated wave-like bending motions of microtubules seen during fast streaming? The general logic we used to analyze this considers the multiple forces that act on cortical microtubules. One is the force kinesins exert directly on a microtubule, a buckling force tangent to its long axis that is resisted by the elastic stiffness of the microtubule. Another force is exerted on the microtubule by the moving cytoplasmic fluid that surrounds it. Thus, the analysis must incorporate the determinants of fluid motion, which include drag from the moving kinesin complexes and from the buckling motions of the microtubules. It is consideration of these coupled effects that allows one to evolve the entire hydrodynamic system in time.

First, consider the magnitude of the force exerted by an individual kinesin motor on its point of attachment to a microtubule. This is equal and opposite to the viscous drag on the motor-cargo complex as it moves toward the plus end. With a motor complex of linear dimension a, the force due to Stokes drag is $3\pi\eta a$v. Assuming a cytoplasmic viscosity, η, of 8 times that of water (27), and an in vivo kinesin velocity, v, of 780 nm/s, the drag force even from a large cargo ($a = 2\mu$m) would be only 0.12 pN; from a small cargo ($a = 60$ nm), it would be 0.007 pN. The force per unit of microtubule length, f_k, generated by a train of kinesin complexes walking along the microtubule can be estimated, because it is proportional to η, v, and, as discussed above, a/d, so that $f_k = \eta v a/d$. This force density is independent of microtubule length up to logarithmic corrections, and the load on a kinesin-cargo complex due to drag is far less than the stall force of kinesin-1 (>5 pN) (28).

We now use these observations to construct a model for the motion of a single minus-end-tethered microtubule interacting with many kinesins in fluid. Consider the multiple forces that act at any point on the microtubule (Fig. 4). As a kinesin steps toward the microtubule plus end, it applies force to the surrounding fluid, and it transfers an equal-opposite force ($\boldsymbol{F}_k$) to the microtubule that is tangent to the microtubule's long axis. Assuming that the microtubule

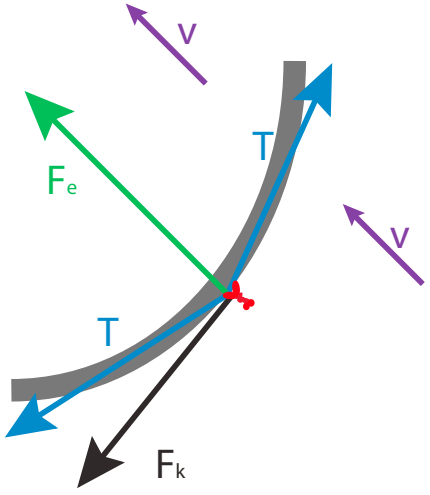

FIGURE 4 Force diagram for a microtubule-kinesin system. A small section of a microtubule (*gray*) is shown being acted on by kinesin forces all along its length that cause bending. A single kinesin (*red*) is shown to focus attention on multiple forces (*arrows*) that act at its point of attachment to the microtubule. A force tangent to the long axis of the microtubule is exerted by kinesins causing a total force along this section of $\boldsymbol{F}_k$. The microtubule has an elastic bending constant that will produce a force ($\boldsymbol{F}_e$) in this section that will oppose the microtubule bending. Tension (T) acts on neighboring elements of the microtubule in opposing directions tangent to the long axis. Force is transferred from the microtubule to the surrounding fluid, which will move at velocity **v**.

is inextensible, the force on the microtubule creates a tension, T, acting on nearby subunits in opposing directions, giving a net force that we denote ΔT. The microtubule has an elastic bending constant, C, that will produce a force, $\boldsymbol{F}_e$, perpendicular to the microtubule long axis. The total local force acting on an element of fluid next to a microtubule is the sum of the above forces,

$$\boldsymbol{f} = \boldsymbol{F}_e + \boldsymbol{F}_k + \Delta T. \quad (1)$$

This equation, supplemented with more detailed expressions for the terms on the righthand side (described below), gives the force acting on a point in the fluid, but this is not enough to determine the motion of the system. Hydrodynamic theory can be used to obtain that motion: The total force acting on an element of liquid has a long-range influence on velocities far from that point. The velocity of the fluid due to a force acting on a point is given by the Oseen tensor (Section S5 in the Supporting Material), which dictates that far from any surfaces, fluid velocity will diminish as the inverse of distance from the point of force, with an additional prefactor of order unity, depending on the force's direction. Conversely, the velocity $\mathbf{u}(\mathbf{r})$ of fluid at an arbitrary point $\mathbf{r}$, is the weighted sum over all forces. In more precise terms, this weight is the Oseen tensor, $\mathbf{J}(\mathbf{r}, \mathbf{r}')$, which connects the force density $\mathbf{f}(\mathbf{r}')$ at point $\mathbf{r}'$ in the fluid to the velocity at another location, $\mathbf{r}$, so that

$$\mathbf{u}(\boldsymbol{r}) = \int \mathbf{J}(\mathbf{r}, \mathbf{r}')\mathbf{f}(\mathbf{r}')d^3r'. \quad (2)$$

The Oseen tensor can also take into account the presence of a wall (e.g., the oocyte cortex) where the velocity vanishes (Supporting Material; Eq. S42). These equations of motion for a microtubule are supplemented with the boundary conditions that the minus end is fixed in space, whereas the plus end is free to move. The implementation of this model is described in detail in Section S5.

Before advancing to a more detailed mathematical analysis, we approximated microtubule motion under simplified physical conditions. Because the $\boldsymbol{F}_k$ kinesin forces are acting, on average, tangent to the microtubule all along its length, they will cause buckling if the microtubule is long enough. To understand this, we can make use of buckling theory for a rod with elastic constant C supporting a load. Consider a section of microtubule of length L. The critical buckling force the load must apply is $f_B = \pi^2 C/L^2$ if the directions of the end segments are not constrained. This will differ by a factor of order unity if there are such end constraints, or if the load is distributed evenly over the rod rather than being confined to its ends. The longitudinal force, f_L, due to kinesin, as discussed above, is $f_L = f_k L$. As L increases, f_L will increase and f_B will decrease. The point at which they are equal gives the value of L at which buckling will first occur. The radius of curvature, R, for buckling will be proportional to L and will occur at $R = (C/\beta f_k)^{1/3}$, where β is a constant that will be determined by a more rigorous analysis outlined below that will allow comparison of theoretical predictions to measured microtubule curvatures in oocytes. We emphasize that this simplified buckling analysis is not precise, because it assumes a static load. With each kinesin force tangent to its local microtubule axis, as a microtubule bends over time, it redirects those forces, implying that the load on the filament is time dependent. We now present a more complete analysis of this dynamic situation.

To understand the motion of a single microtubule, one must consider that the surrounding fluid creates drag on it. We first consider a single microtubule with a local drag coefficient ν, but with no long-range hydrodynamics. A full hydrodynamic treatment must include the motions of kinesins on many adjacent microtubules and the more complex flow field they generate. However, for a simple single-microtubule simulation, we will assume that the only effect of the other microtubules is to produce a constant fluid velocity field, v_s, which we will regard as a fixed external parameter. We show in Section S5.7 in the Supporting Material that this approximation of local drag is in good agreement with the full hydrodynamic treatment for a single microtubule system.

The single-microtubule dynamics model is developed in detail in Section S4 in the Supporting Material. It is similar to one developed previously for filament bending in gliding assays on glass surfaces coated with motors (29). However, our model is three-dimensional in an external fluid velocity field, rather than two-dimensional with no external velocity field. The configuration of the microtubule, $\mathbf{r}(s)$, is parameterized as a function of arclength, s. Assuming that drag is only local, and writing out the forces on the righthand side of Eq. 1 explicitly,

$$\nu\frac{\partial \mathbf{r}}{\partial t} = -C\frac{\partial^4 \mathbf{r}}{\partial s^4} + \frac{\partial}{\partial s}\left(T(s)\frac{\partial \mathbf{r}}{\partial s}\right) - f_k\frac{\partial \mathbf{r}}{\partial s} + \nu v_s \hat{k}, \quad (3)$$

where the position-dependent tension, $T(s)$, enforces the inextensibility of the chain $|\partial \mathbf{r}/\partial s| = 1$.

We can now use Eq. 3 to determine the three-dimensional motion of a microtubule subjected to kinesin forces while its minus end is tethered in free space. Mathematical analysis yields a set of traveling wave solutions for long chains (Sections S4.1–S4.4 in the Supporting Material). The equation for their shape can be mapped onto the equation for a spherical pendulum, and their form can be analyzed in several situations. For the case $v_s = 0$, there are circularly rotating solutions with angular velocity $f_k/(\nu R)$, where R is the radius of curvature (Supporting Material; Eq. S24). We have studied numerically how R depends on the fluid velocity field and found that it is quite insensitive over a wide range of v_s velocities. The precise value of R is determined by the boundary conditions, so we applied boundary conditions numerically that held the

minus end at a fixed location but allowed it to pivot, whereas the plus end was completely free. Starting from random initial conditions, the equation rapidly goes to a steady state that typically is described by a curve that asymptotically becomes a helix that rotates uniformly at constant angular velocity ω (Fig. 5; Movie S4). The crumpled initial conditions are clearly not attainable with a real microtubule, but they are shown to demonstrate that even from such extreme starting configurations, the dynamics approach the same helical solution. The handedness that develops for the helix is random, but is stable once steady state is attained. A combination of this numerical work and our analytical results agrees with our much simpler buckling analysis, discussed above, that gives $R = (C/\beta f_k)^{1/3}$; it also agrees with the power law found previously (29). However, now we can determine that $\beta = 0.05 \pm 0.0005$. The asymptotic radius varies only slightly over a wide v_s flow field velocity range (Section S4.6 in the Supporting Material).

To move closer to the situation for a single microtubule in an oocyte, we studied variants of this model in which the boundary condition of the tethered minus end is altered such that it is no longer freely hinged about a fixed point, but is rigidly oriented in one direction, as if rooted in and projecting away from the cortex. Because of the stiffness of the microtubule, this shifts bending for the first circular turn away from the minus end. We also studied the influence of a barrier to motion that is similar to the oocyte cortex by adding a short-ranged repulsive wall potential that is positioned near the minus end and is parallel with the flow field (Section S4.6 in the Supporting Material). This still allows traveling waves, but for most values of the imposed fluid flow velocity, v_s, the waves evolve into flattened cycloidal or sinusoidal configurations parallel to the barrier (Movie S5). This behavior can also be understood in detail analytically, in excellent agreement with the simulations (Section S4.4 in the Supporting Material).

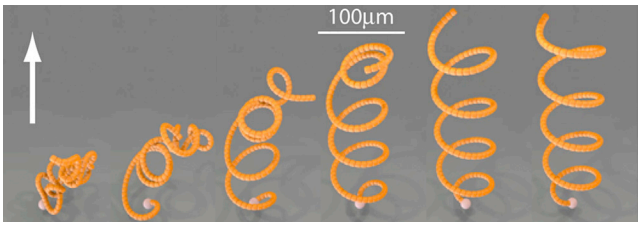

FIGURE 5 Single-filament bending behavior generated by kinesin forces and an externally imposed fluid flow. Six time points from a 200 frame simulation of a microtubule-like filament with its minus-end (*white ball*) fixed in space but free to pivot (see Movie S4 and Section S4.6). Starting from initial random compressed configurations of the filament (*left side*), tangent forces from kinesins walking toward the free plus end, combined with an externally imposed fluid flow field (*arrow*) generates a stable rotating helical wave. Reasonable values for microtubule stiffness, kinesin force, and fluid viscosity produce a final radius of curvature between 25 and 54 μm. For viewing purposes, the diameter of the filament here is 2000-fold that of a real microtubule.

Self-organization of many microtubules using simulation

For a more complete model of microtubule behavior in oocytes, the same physical ingredients were considered, but with an array of 100 filaments tethered by their minus ends near a cortex-like barrier plane at which both fluid and filament velocities must be zero. Also, fluid flows were generated internally by kinesin motion toward plus ends, rather than being externally imposed. Thus, kinesin force and microtubule motion coupled to the surrounding cytoplasmic fluid should generate a complete hydrodynamic model as described by Eqs. 1 and 2. Constant kinesin velocity toward plus ends was combined with Eq. 2 to evolve the system in time. The added complexity of this system pushed solutions beyond the scope of current analytic treatments, but it could be modeled numerically (Section S5 in the Supporting Material). This model was unexpectedly predictive, giving rise to an order-disorder transition between two states similar to those observed in slow- and fast-streaming oocytes. To determine whether it is robust, repeated simulations with various parameter changes were used to focus on three general questions: 1) How can a collection of many noncorrelated microtubules that is being acted on by kinesin forces spontaneously self-organize into aligned arrays and undergo correlated bending as observed in fast streaming?, 2) Can parameter changes within the model explain the disorder-to-order transition?, and 3) If so, what parameters most directly influence that transition?

In simulations, microtubule-like filaments were modeled with free-rotating minus ends tethered at height H above the cortex-like barrier, representing a height at which microtubules that are constrained by minus-end segments rooted in the cortex could bend enough to lie parallel with it. The semiflexible nature of the filaments and their interactions with each other were ensured by modeling them as chains of balls with spring potentials between them and with next-nearest-neighbor repulsive potentials. The equilibrium distance between adjacent balls in a chain was 1 in the units used for the simulation. In Fig. 6, A and B, adjacent minus-end tether points are separated by 2 units, and chain lengths are 16 units. Two distinct behaviors of the system emerged in simulations. First, at intermediate kinesin force density on the filaments, and with filament tether points close to the cortical barrier (e.g., $H = 1.0$), bending dynamics did not become well ordered (Fig. 6 A; Movie S6). Small groups of filaments did correlate over short distances for brief times, creating patterns similar to those observed for microtubules in slow-streaming oocytes (Fig. 6 C; Movie S1), but long-range correlations did not develop. In the second behavior, increasing the distance between the filament tether points and the cortical barrier ($H = 2.0$) while holding all

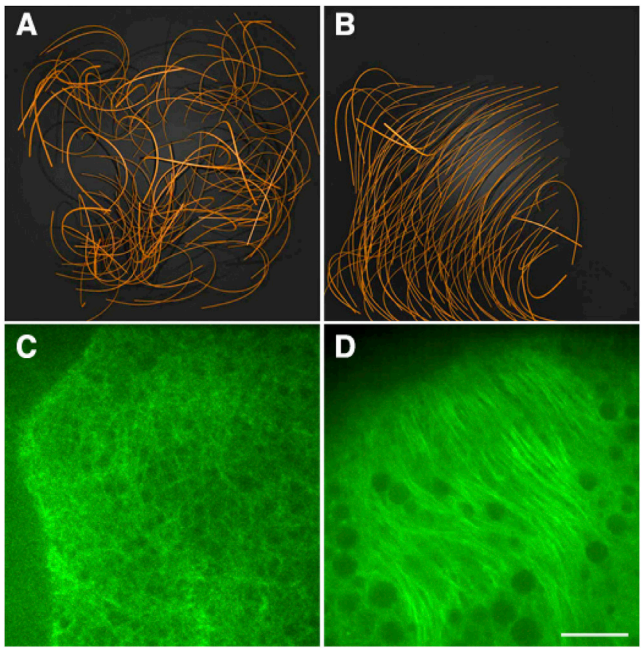

FIGURE 6 Correlated microtubule-array bending generated by kinesin shear force between fluid and filaments near a barrier plane. (*A* and *B*) Views from above of arrays of 100 microtubule-like filaments with minus-end pivot points at two distances from the cortical barrier, (*A*) $H = 1.0$ (see Movie S6) and (*B*) $H = 2.0$ (see Movie S7). These are outcomes after 200 iterations of simulations under conditions of 1) spacing between minus-end pivot points of 2 units; 2) initial randomized filament configurations; 3) kinesin-like fluid-filament shear forces tangent to each filament axis at all points; and 4) cytoplasmic fluid movements generated by the kinesin-filament shear forces. Note the largely noncorrelated bending behavior in (*A*) versus the correlated bending behavior in (*B*). (*C* and *D*) Shown are confocal images of GFP-α-tubulin at 0–10 μm depth beneath the oocyte membrane. Scale bar, 10 μm. (*C*) Stage 10A slow streaming (see Movie S1). (*D*) Stage 10B fast streaming (see Movie S2).

other parameters unchanged resulted in a striking self-organization into uniformly oriented bending arrays that lay parallel to the barrier (Fig. 6 B; Movie S7). Some filaments at the array edges, where there were few neighbors, exhibited independent helical behaviors akin to those of single filaments (Fig. 5; Movie S4), but those with a full set of neighbors exhibited strongly correlated bending dynamics similar to those of microtubules in fast-streaming oocytes (Fig. 6 D; Movie S2). When H was held at 2.0 while shifting other parameters to create much higher force density on microtubules, the first noncorrelated slow-streaming-like state was reproduced. Those parameter changes included increased kinesin velocity (v_0), larger kinesin-cargo diameter (a; increased drag), reduced spacing between kinesin-cargo complexes (d), or increased viscosity (η). This outcome could also result from decreased microtubule stiffness (C). Alternatively, parameter changes that resulted in much lower force density allowed evolution of correlated microtubule behavior, but substantially delayed its attainment and reduced the associated fluid velocity ($v(r)$). Those parameter changes included reduced kinesin velocity, smaller cargo diameter, increased cargo spacing, decreased viscosity, or increased microtubule stiffness. Repeated trials identified parameter values that favored correlated behavior and high fluid velocity: intermediate filament stiffness akin to that measured for microtubules (30,31), intermediate kinesin force density along the filaments, and minus-end pivot points above the wall at a distance equivalent to the spacing between microtubule minus ends. At a spacing of 2 units between microtubule tether points combined with the intermediate values for stiffness and force density, the transition between weak and strong correlation occurred near a height of $H = 1.5$ units for chain lengths of 16 and 32, and for filament populations of 50 and 100. Thus, along with stiffness of microtubules and force density on them, the distance away from the cortex at which microtubules can form a parallel layer is a parameter that could control the transition from slow disordered to fast ordered streaming.

The subcortical microtubule layer is anchored

One key assumption for our model that is debatable is that the minus ends of microtubules that form the bending subcortical arrays are tethered to the cortex. Consistent with this, early studies showed that microtubule regrowth after depolymerization begins at the oocyte cortex (13). However, it was seen later that although γ-tubulin, which is a minus-end binding and nucleation factor, is concentrated in the cortex during slow streaming, it is not concentrated there during fast streaming, raising the possibility that microtubule minus ends are released from cortical anchors at the transition to fast streaming (15,16,32).

If the minus ends of oocyte microtubules are released from the cortex at the transition to fast streaming, they should be carried along by the fast cytoplasmic flows. To test this, we analyzed GFP-tubulin dynamics by FRAP in stage 10B oocytes using a two-photon microscope. Well-aligned bands of subcortical microtubules were marked by photobleaching within a shallow optical section; then, the positions of the bleached zone and streaming yolk granules were observed by time-lapse imaging. If minus ends are not tethered, such a bleached mark should move along with organelles in the cytoplasmic flow. The shallow bleached zones recovered fluorescence in a symmetrical fashion and they made no discernible shifts in position, despite fast flow of yolk granules through them (Fig. 7; Movie S8). This shows that subcortical microtubule arrays are not carried along by fast cytoplasmic streaming flows, indicating that they are indeed tethered to the cortex, consistent with the assumption used for our model.

Comparison to microtubule bending in oocytes

The fact that simulations with a full range of parameter variations led to two states of microtubule organization similar to those seen in oocytes suggests that the model represents

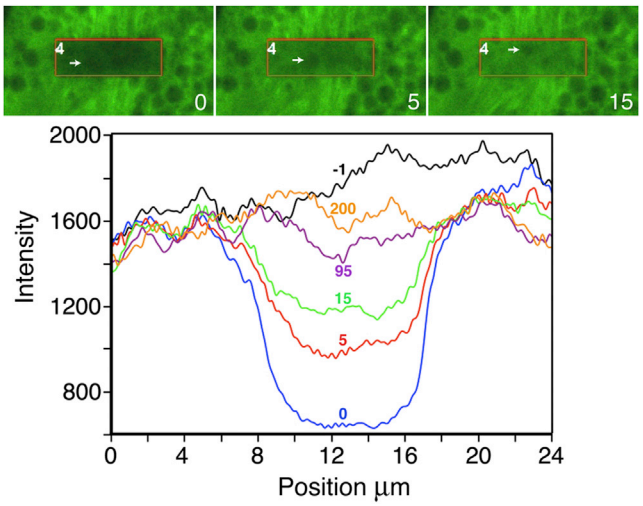

FIGURE 7 Subcortical arrays of microtubules are stationary during streaming. (*Top*) Subcortical GFP-tubulin in a stage 10B oocyte imaged by time-lapse two-photon fluorescence microscopy. Intense two-photon excitation was used to photobleach a 10 × 30 μm area (*orange box*) in a shallow optical section of well-aligned subcortical microtubules. White arrows mark the positions of a yolk granule carried by fast streaming at ~300 nm/s. (*Bottom*) Fluorescence intensity was scanned from bottom (0 μm) to top (24 μm) of images at various time points (noted in seconds). The bleached zone did not move laterally, and fluorescence recovery was symmetrical, despite streaming of cytoplasm through the area (see Movie S8).

the streaming mechanism well. To test the model further, the wave-like bending behaviors in model simulations were compared to real microtubule bending behavior in oocytes. We examined analytical solutions of single-microtubule bending using elastic constants for microtubules of $C = 0.5$ to 2×10^{-23} Nm^2, as reported previously (30,31) (Section S4.6 in the Supporting Material). With a kinesin velocity of 780 nm/s, a cargo diameter/spacing (a/d) between 0.4 and 1, and assuming a cytoplasmic viscosity in fast-streaming oocytes of 8 times that of water (27), the radius of curvature, R, is predicted to be 25–54 μm, and the wave period, τ, is predicted to be 203–1094 s. For comparison, we measured bending behaviors of GFP-tubulin microtubule arrays during fast streaming in stage 10B–11 oocytes. Array trajectories had varying degrees of curvature, and the curves oscillated in a sinusoidal fashion (Figs. 1 D and 6 D; Movie S2). Focusing on the most acute peaks, curve radii were estimated by fitting with circles of known diameter. The average minimum curvature radius was $R = 16.3 \pm 2.2$ μm, mean ± SE of $n = 6$ oocytes (30 arrays), which is reasonably close to the 25 μm minimum predicted by the model. To estimate wave periods, τ, in oocytes, the amount of time for a complete wave form to pass a fixed point was determined for arrays that remained suitably in the optical section. The average was 370 ± 42s, mean ± SE of $n = 6$ oocytes (19 arrays). This is within the period range predicted, indicating that our model's physical explanation for oocyte microtubule bending is valid.

Reducing kinesin-generated forces slows streaming flows and hinders microtubule alignment

The many-filament model, which is based on fundamental physical principles, shows self-organizing fast streaming behavior similar to that seen in oocytes. For an additional test, we studied the effects of reducing kinesin-generated force density on cortical microtubules. As noted above, the prediction is that reduced force density will delay attainment of the correlated fast-streaming state and will result in reduced fluid velocity in that state. Considering the possibility that kinesin-1 concentration is a limiting factor, we attempted to reduce force density by eliminating one copy of the *Khc* gene, which is known to reduce the concentration of Khc protein (33). Stage 10B–11 oocytes heterozygous for a 60 kb deletion that removes the *Khc* gene (*Df(2R)BSC309/+*) did not show signs of delayed entry into fast streaming, and although the average velocity of fast-streaming endosomes was somewhat reduced, that change was not significant (Fig. 8 A). This suggests that even with half of the normal gene dosage in the female germline, Khc concentration in oocytes is not limiting for the fast-streaming pattern or velocity. This is consistent with prior observations that heterozygous *Khc*

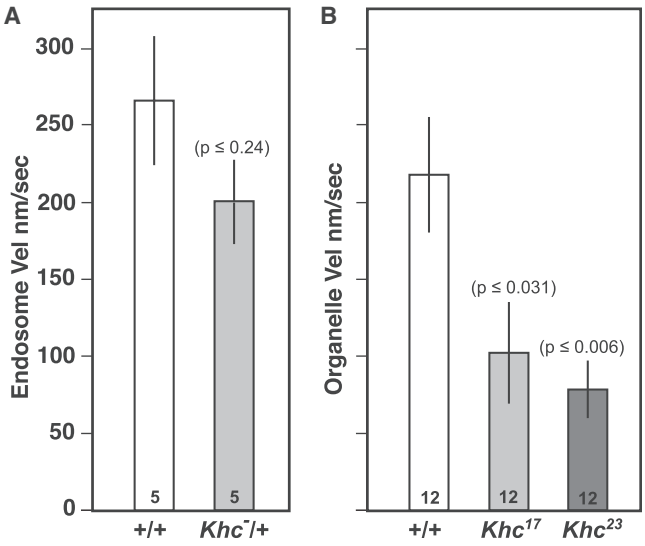

FIGURE 8 Tests of reduced kinesin force density on microtubules in fast streaming. (*A*) The velocities of dye-loaded subcortical endosomes measured in stage 10B–11 oocytes from females with two copies (+/+) or one copy (Khc^-/+) of the *Khc* gene. (*B*) Velocities of subcortical organelles in oocytes that were expressing GFP-tubulin. Organelles that exclude GFP-tubulin were tracked in stage 10B–11 oocytes that were wild-type (+/+) or that had been rendered homozygous for a *Khc* mutant allele (Khc^{17} or Khc^{23}), which are known to slow the movement of kinesin-1 on microtubules (33). Velocity analysis was done only in mutant oocytes that displayed correlated fast-streaming patterns of motion. Sample sizes (number of oocytes) are shown in each bar and variance is the standard error. *p*-Values reflect the comparison to +/+ using a two-tailed *t*-test with unequal variance.

null mutations do not alter kinesin-1-driven transport processes, even in the long narrow confines of neuronal axons (21).

Using another approach, we took advantage of two well-characterized recessive lethal alleles of *Khc* that cause 3.8-fold (Khc^{23}) and 1.6-fold (Khc^{17}) slowing of motor velocity on microtubules in vitro (33) by changing single amino acids in the force-generating head domain of kinesin. To study their influences, females expressing GFP-tubulin and heterozygous for a mutant allele were induced to undergo mitotic recombination in their germline stem cells such that egg chambers descended from them were homozygous for the mutant allele (9,11). In stage 10B–11 mutant oocytes, three different streaming behaviors were observed: 1) noncorrelated behavior and slow flow velocities for GFP-excluding organelles (Khc^{23}, 26 $\pm$ 5 nm/s, mean $\pm$ SE of $n = 12$ oocytes; Khc^{17}, 38 $\pm$ 6 nm/s, mean $\pm$ SE of $n = 12$ oocytes); 2) faint patches of correlated microtubules with ordered streaming flows; and 3) more extensive, but still faint, subcortical microtubule arrays with uniform correlated streaming flows at velocities that were significantly less than those seen in controls (Fig. 8 B). These observations are consistent with the delayed self-organization and slowed fluid velocity predicted by the model for reduced force density on microtubules.

DISCUSSION

In general, processes involving the transport of cargoes with a strong directional bias should be profoundly affected by hydrodynamic principles, because at low Reynolds number the motions of distant objects are coupled through viscous drag. Elegant studies by Hamaguchi and Hiramoto in sand dollar zygotes established that length-dependent pulling forces on astral microtubules emanating from the centrosome of the male pronucleus move it toward the cell center (34). They suggested that such forces are generated by drag on trains of organelles as they are carried by microtubule motors toward minus ends that are attached to the centrosome. It has since been shown that drag on dynein-cargo complexes indeed generates important length-dependent pulling forces on microtubules whose minus ends are attached to pronuclei (35–37). Our work has focused on what is in essence the reverse process: predominantly plus-end-directed transport driven by kinesin-1 along microtubules that are attached by their minus ends to the oocyte cortex. In contrast to the microtubule straightening-pulling effects of dynein cargoes walking toward anchored minus ends, drag on kinesin cargoes moving away from anchored minus ends causes microtubules to buckle and, under some conditions, to self-organize into parallel arrays that bend in a correlated fashion. The equal-opposite kinesin force transferred to cytoplasm drives long-range fluid flows in varying directions dictated by the bending arrays, which mixes the cytoplasm.

In developing oocytes, the timing of the switch from mid-stage slow streaming to late-stage fast streaming is crucial. If fast streaming occurs too early, the proper concentration and anchorage of key body-axis determinants at their cortical sites fails and subsequent embryo development proceeds without normal patterning (8,38). On the other hand, if streaming-mediated mixing does not occur, embryos do not develop normally (11). Our hydrodynamic modeling shows that oocytes could control the slow- to fast-streaming transition by changing H, the distance between the cortical barrier plane and the level at which cortically tethered microtubules can align parallel to it. This is because fluid motion between the barrier plane and the microtubule layer makes an important contribution to hydrodynamic coupling of microtubules and thus to their correlated bending behavior. Since for fast streaming, the predicted optimum distance of microtubule arrays from the barrier is approximately twice the spacing between microtubule minus ends, if a shift away from the cortex is a trigger for correlation, it need not be large. High-resolution fluorescence images of stage 9 oocytes (12) suggest a spacing between cortical microtubules of ~1 μm. Thus, a spacing increase between the cortex and the subcortical microtubule layer of just 1 μm could be sufficient to allow the switch to correlated fast streaming. Evidence consistent with a multimicron inward shift of microtubules during the transition from slow to fast streaming has been reported (16). How such a shift could be accomplished while keeping minus ends tethered is an interesting question. One possibility is that if the initial segments of microtubules are rigidly oriented at an average angle perpendicular to the cortex, changes in stiffness could increase the radius over which they could bend to form a subcortical layer. Alternatively, an increase in cortical microtubule density that reduces spacing between them could accomplish the transition without a subcortical shift. Future ultrastructural analysis of the organization of microtubules in and near the cortex before and after the transition should provide important insights into whether or not changes in H or cortical microtubule density contribute to the control mechanism.

Other model parameters could also influence the slow- to fast-streaming transition, including average kinesin-cargo size, spacing between cargoes along microtubules, kinesin velocity, cytoplasmic viscosity, or microtubule stiffness. We have shown that slow kinesin mutations hinder self-organization and reduce fast-streaming velocity, as predicted. Consistent with viscosity changes being important, destabilizing the cytoplasmic f-actin meshwork, which should decrease viscosity, stimulates premature fast streaming in stage 8–9 oocytes (8,13,15,38) and hyperstabilizing the f-actin meshwork has been shown to prevent fast streaming in stage 11 oocytes (15).

Interestingly, model simulations show that increasing the separation distance between the subcortical microtubule layer and the cortical wall (beyond 2 units) facilitates rapid

alignment into parallel arrays, but the amplitude of bending becomes less. Considering the purpose of fast streaming in oocytes, mixing of cytoplasm, this suggests that the transition from slow to fast states resets the system to the edge of a symmetry-breaking phase where there is sufficient order to align microtubules and generate robust cytoplasmic flow velocity, yet enough bending of the arrays to facilitate semichaotic variations in flow direction. In regard to a need for flow-pattern variation, rigorous analysis in two dimensions using the Thurston-Nielsen classification theorem has shown that topological chaos is crucial for efficient fluid mixing (39). This is particularly the case for the low-Reynolds-number regime (small scale and high viscosity) that exists in an oocyte. Thus, control of stage 10B parameters to encourage both fast flows and bending is likely an important element for successful mixing of nurse cell and oocyte cytoplasms. Another important consideration for mixing is that the hemispherical geometry of the oocyte cortex must introduce additional instabilities in microtubule array correlation and flow patterns. Simulations of streaming inside hemispheres will be computationally demanding but should produce additional insights into the biophysical mechanism of cytoplasmic-streaming-driven mixing.

SUPPORTING MATERIAL

Supporting Materials and Methods, sixteen figures, and eight movies are available at http://www.biophysj.org/biophysj/supplemental/S0006-3495(16)30121-7.

AUTHOR CONTRIBUTIONS

W.M.S. and J.M.D. conceived and designed the project. C.E.M., I.D., A.M.B., and W.M.S. planned, executed, and analyzed oocyte experiments. M.E.B. and J.M.D. developed the physical model and microtubule bending streaming simulations. C.E.M., W.M.S., and J.M.D. wrote the manuscript with input from I.D., M.E.B., and A.M.B.

ACKNOWLEDGMENTS

For critical thinking and invaluable comments on the model and manuscript, we thank Bill Sullivan, Susan Strome, Doug Kellogg, and Dick McIntosh.

This work was supported by National Institutes of Health grant GM46295 (to W.M.S.), funds from the University of California, Santa Cruz, and National Science Foundation CCLI grant DUE-0942207 (to J.M.D.).

REFERENCES

1. Vale, R. D., and R. A. Milligan. 2000. The way things move: looking under the hood of molecular motor proteins. *Science.* 288:88–95.
2. Cooley, L., and W. E. Theurkauf. 1994. Cytoskeletal functions during *Drosophila* oogenesis. *Science.* 266:590–596.
3. Ephrussi, A., and R. Lehmann. 1992. Induction of germ cell formation by oskar. *Nature.* 358:387–392.
4. Berleth, T., M. Burri, …, C. Nüsslein-Volhard. 1988. The role of localization of bicoid RNA in organizing the anterior pattern of the *Drosophila* embryo. *EMBO J.* 7:1749–1756.
5. Kim-Ha, J., J. L. Smith, and P. M. Macdonald. 1991. *oskar* mRNA is localized to the posterior pole of the *Drosophila* oocyte. *Cell.* 66:23–35.
6. Riechmann, V., and A. Ephrussi. 2001. Axis formation during *Drosophila* oogenesis. *Curr. Opin. Genet. Dev.* 11:374–383.
7. Gutzeit, H. O., and R. Koppa. 1982. Time-lapse film analysis of cytoplasmic streaming during late oogenesis of *Drosophila*. *J. Embryol. Exp. Morphol.* 67:101–111.
8. Theurkauf, W. E. 1994. Premature microtubule-dependent cytoplasmic streaming in cappuccino and spire mutant oocytes. *Science.* 265:2093–2096.
9. Brendza, R. P., L. R. Serbus, …, W. M. Saxton. 2000. A function for kinesin I in the posterior transport of oskar mRNA and Staufen protein. *Science.* 289:2120–2122.
10. Palacios, I. M., and D. St Johnston. 2002. Kinesin light chain-independent function of the Kinesin heavy chain in cytoplasmic streaming and posterior localisation in the *Drosophila* oocyte. *Development.* 129:5473–5485.
11. Serbus, L. R., B. J. Cha, …, W. M. Saxton. 2005. Dynein and the actin cytoskeleton control kinesin-driven cytoplasmic streaming in *Drosophila* oocytes. *Development.* 132:3743–3752.
12. Parton, R. M., R. S. Hamilton, …, I. Davis. 2011. A PAR-1-dependent orientation gradient of dynamic microtubules directs posterior cargo transport in the *Drosophila* oocyte. *J. Cell Biol.* 194:121–135.
13. Theurkauf, W. E., S. Smiley, …, B. M. Alberts. 1992. Reorganization of the cytoskeleton during *Drosophila* oogenesis: implications for axis specification and intercellular transport. *Development.* 115:923–936.
14. Brendza, R. P., L. R. Serbus, …, J. B. Duffy. 2002. Posterior localization of dynein and dorsal-ventral axis formation depend on kinesin in *Drosophila* oocytes. *Curr. Biol.* 12:1541–1545.
15. Dahlgaard, K., A. A. Raposo, …, D. St Johnston. 2007. Capu and Spire assemble a cytoplasmic actin mesh that maintains microtubule organization in the *Drosophila* oocyte. *Dev. Cell.* 13:539–553.
16. Wang, Y., and V. Riechmann. 2008. Microtubule anchoring by cortical actin bundles prevents streaming of the oocyte cytoplasm. *Mech. Dev.* 125:142–152.
17. Yu, Y. V., Z. Li, …, M. A. Welte. 2011. Targeting the motor regulator Klar to lipid droplets. *BMC Cell Biol.* 12:9.
18. Meijering, E., O. Dzyubachyk, and I. Smal. 2012. Methods for cell and particle tracking. *Methods Enzymol.* 504:183–200.
19. Berg, H. C. 1983. Random Walks in Biology. Princeton University Press, Princeton, NJ.
20. Purcell, E. M. 1977. Life at low Reynolds number. *Am. J. Phys.* 45:3–11.
21. Pilling, A. D., D. Horiuchi, …, W. M. Saxton. 2006. Kinesin-1 and Dynein are the primary motors for fast transport of mitochondria in *Drosophila* motor axons. *Mol. Biol. Cell.* 17:2057–2068.
22. Zimyanin, V. L., K. Belaya, …, D. St Johnston. 2008. In vivo imaging of *oskar* mRNA transport reveals the mechanism of posterior localization. *Cell.* 134:843–853.
23. Shubeita, G. T., S. L. Tran, …, S. P. Gross. 2008. Consequences of motor copy number on the intracellular transport of kinesin-1-driven lipid droplets. *Cell.* 135:1098–1107.
24. Kural, C., H. Kim, …, P. R. Selvin. 2005. Kinesin and dynein move a peroxisome in vivo: a tug-of-war or coordinated movement? *Science.* 308:1469–1472.
25. Cai, D., K. J. Verhey, and E. Meyhöfer. 2007. Tracking single Kinesin molecules in the cytoplasm of mammalian cells. *Biophys. J.* 92:4137–4144.
26. Amos, L. A. 1987. Kinesin from pig brain studied by electron microscopy. *J. Cell Sci.* 87:105–111.
27. Luby-Phelps, K. 2000. Cytoarchitecture and physical properties of cytoplasm: volume, viscosity, diffusion, intracellular surface area. *Int. Rev. Cytol.* 192:189–221.

28. Svoboda, K., and S. M. Block. 1994. Force and velocity measured for single kinesin molecules. *Cell.* 77:773–784.

29. Bourdieu, L., T. Duke, …, A. Libchaber. 1995. Spiral defects in motility assays: a measure of motor protein force. *Phys. Rev. Lett.* 75:176–179.

30. Felgner, H., R. Frank, and M. Schliwa. 1996. Flexural rigidity of microtubules measured with the use of optical tweezers. *J. Cell Sci.* 109:509–516.

31. Gittes, F., B. Mickey, …, J. Howard. 1993. Flexural rigidity of microtubules and actin filaments measured from thermal fluctuations in shape. *J. Cell Biol.* 120:923–934.

32. Cha, B. J., L. R. Serbus, …, W. E. Theurkauf. 2002. Kinesin I-dependent cortical exclusion restricts pole plasm to the oocyte posterior. *Nat. Cell Biol.* 4:592–598.

33. Brendza, K. M., D. J. Rose, …, W. M. Saxton. 1999. Lethal kinesin mutations reveal amino acids important for ATPase activation and structural coupling. *J. Biol. Chem.* 274:31506–31514.

34. Hamaguchi, M. S., and Y. Hiramoto. 1986. Analysis of the role of astral rays in pronuclear migration in sand dollar eggs by the Colcemid-UV method. *Dev. Growth Differ.* 28:143–156.

35. Kimura, K., and A. Kimura. 2011. Intracellular organelles mediate cytoplasmic pulling force for centrosome centration in the *Caenorhabditis elegans* early embryo. *Proc. Natl. Acad. Sci. USA.* 108:137–142.

36. Longoria, R. A., and G. T. Shubeita. 2013. Cargo transport by cytoplasmic Dynein can center embryonic centrosomes. *PLoS One.* 8:e67710.

37. Shinar, T., M. Mana, …, M. J. Shelley. 2011. A model of cytoplasmically driven microtubule-based motion in the single-celled *Caenorhabditis elegans* embryo. *Proc. Natl. Acad. Sci. USA.* 108:10508–10513.

38. Manseau, L., J. Calley, and H. Phan. 1996. Profilin is required for posterior patterning of the *Drosophila* oocyte. *Development.* 122:2109–2116.

39. Thurston, W. 1988. On the geometry and dynamics of diffeomorphisms of surfaces. *Bull. Am. Math. Soc.* 19:417–431.

Biophysical Journal, Volume *110*

Supplemental Information

A Mechanism for Cytoplasmic Streaming: Kinesin-Driven Alignment of Microtubules and Fast Fluid Flows

Corey E. Monteith, Matthew E. Brunner, Inna Djagaeva, Anthony M. Bielecki, Joshua M. Deutsch, and William M. Saxton

Supporting Material

A mechanism for cytoplasmic streaming: Kinesin-driven alignment of microtubules and fast fluid flows.

Corey E. Monteith, Matthew E. Brunnner, Inna Djagaeva, Anthony Bielecki, Joshua M. Deutsch, William M. Saxton

1 Movie Legends

Movie S1

Weak correlation of microtubule motion and bending during slow cytoplasmic streaming. Live stage 9 Drosophila oocytes containing GFP-α-tubulin expressed in the germline were dissected, mounted in halocarbon oil, and fluorescence was recorded at $5sec$ intervals using an inverted Ultraview spinning disk confocal microscope. The image series is played back here at 30 $frames/sec$. The optical section is $5-10\mu m$ inward from the oocyte membrane (see Fig. 1A,B).

Movie S2

Strong correlation of microtubule motion and bending behavior during fast cytoplasmic streaming. GFP-tubulin fluorescence images were recorded in Stage 10B oocytes at $5sec$ intervals and are played back at 30 $frames/second$ (see Fig. 1C,D). The optical section, $5-10\mu m$ inward from the oocyte membrane, cuts through subcortical cytoplasm in some areas, producing

views of bright, ordered parallel arrays of undulating microtubules and of fast moving yolk endosomes (dark spheres). In other areas, where the section is shallower and cuts through the cortex, yolk endosomes associated with the cortex move slowly in the directions of overlying fast flows.

Movie S3

Endosome and lipid droplet fast streaming motion. Time-lapse confocal fluorescence images of a stage 10B oocyte showing endosomes containing trypan blue dye (red fluorescence) and lipid droplets tagged with GFP-LD (green fluorescence) expressed just in the germline. Images were collected in both channels at 2 *sec* intervals, and are played back at 30 $Frames/sec$. The oocyte nucleus is seen as a dark sphere in the top left. Note the varying fast streaming flow patterns.

Movie S4

A simulation of single filament bending behavior induced by kinesin forces. The filament has microtubule-like stiffness and forces tangent to its axis at all points like those generated by kinesin-cargo complexes moving through cytoplasm toward the free plus-end (see Fig. 5 and Supporting Material 4.6). Those plus-end directed walking forces, if unopposed, would propel the filament with its minus end leading, but its minus-end (white sphere) is tethered in space. It can rotate, but not translate. A second force, representing a cytoplasmic streaming flow field is imposed on the system, moving constantly from the bottom to the top of the field of view. Repeated simulations consistently developed stable rotating helical wave forms, with handedness depending on the details of random initial filament configurations. Analytical solutions with reasonable values for microtubule stiffness, and kinesin force predict a radius of curvature of $24 - 54\mu m$, which is roughly one third the width of a stage 10B oocyte. To facilitate recognition of the bending behavior, the width of the filament here is scaled up to 2,000-fold that of a real microtubule.

Movie S5

A simulation of single filament bending behavior when adjacent to an impenetrable wall. These parameters are the same as in Movie S4 but the system differs by the addition of a barrier that is parallel to the microtubule. This changes the travelling helical wave to a shape similar to a sinusoidal wave that is very well described by the mathematical analysis of Sec. 4.4. When the cytoplasmic streaming flow field is slower, the shape becomes similar to prolate cycloids that are also well described by the same analysis.

Movie S6

A simulation of the bending behaviors of 100 filaments with minus-ends tethered near a barrier to filament and fluid motions. The axis of each filament is initially in a random configuration (see Fig. 6A and Supporting Material Sec. 5.11)) that changes due to interactions of microtubule-like stiffness, kinesin-like fluid-filament shear forces tangent to each filament at all points, and hydrodynamics as described in the Supporting Material, Sec. 5 (parameters as in Fig. S16(d)). Filament length is 16 (dimensionless units), at an elevation of $H = 1$ above a membrane-like wall. The velocity field at the wall vanishes, which suppresses hydrodynamic interactions between microtubules. In this case, the elevation of minus-ends is too low to allow for long-range filament correlation and organized fast streaming.

Movie S7

A simulation of the bending behaviors of 100 filaments with elevated minus end tether points. The parameters are as described for Movie S6, except that minus-ends are tethered above the membrane barrier at $H = 2$ (see Fig. 6B; parameters as in Fig. S16c). In this case fluid motion between the minus-ends and the wall allow strong hydrodynamic interactions between microtubules that create long-range correlated behaviors and robust fast streaming. At higher minus-end tethering elevations, correlation becomes stronger and microtubule bending behavior is diminished, generating relatively straight stable arrays.

Movie S8

FRAP evidence for cortical tethering of microtubules. High magnification GFP-tubulin images recorded with an Olympus 2-photon microscope in a stage 10B oocyte at 0.93 *sec* intervals are played back here at 30 $frames/sec$. High intensity excitation was used to photobleach a shallow $10 \times 30 \mu m$ area in subcortical arrays of microtubules. Note that the photobleached area remains stationary as fluorescence recovers, while organelles that exclude GFP-tubulin stream past. Adjacent non-streaming organelles are associated with the cortex. Quantification and other details of this experiment are presented in Fig. 7.

2 Enhancement of Streaming Due to Hydrodynamics

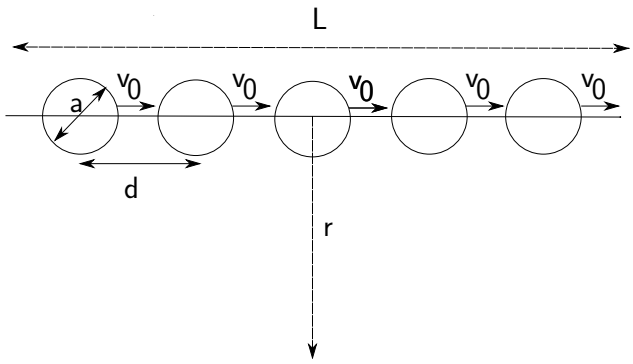

Figure S1: **Fluid movement by viscous drag on a train of impellers at low Reynolds number.** A train of spherically shaped impellers of diameter a and separation d, all moving in a fluid with a velocity v_0. The velocity $v(r)$ is measured at a point a distance r from the axis.

Consider objects that can move surrounding fluid by viscous drag, referred to as "impellers" here. Each impeller has a maximum linear dimension a, and has a mean spacing of d, arranged in a straight line as shown in Fig S1, reproduced from Fig 2 of our accompanying paper. These impellers are pictured as spheres, but hydrodynamics is not sensitive to the exact shape of an

impeller, as it depends mainly on its maximum linear dimension [18]. We will now analyze the amount of streaming due to motion of these impellers moving on a single microtubule. We initially consider the impellers to be much larger than the kinesin molecules so that they dominate the hydrodynamical response of the fluid.

If spherical impellers were close-packed along the microtubule, that is $a \approx d$, then this problem would be equivalent to a single rod of length L moving at constant velocity v_0 in the fluid in a direction parallel to its long axis. In that case, the velocity field for distances $r \ll L$ has only a weak logarithmic dependence of r, meaning that up to a correction of order $\ln(L/a)$, the velocity field is only weakly dependent on distance and for most practical cases will differ by less than an order of magnitude from v_0. Here we take the velocity of the fluid, $v(r)$, to go to zero far from the rod. This is related to the well known result that the drag on a rod of length L will only differ by a logarithmic factor from that of a sphere of diameter L despite the latter's much greater volume [18]. Such a system of densely packed impellers would be very efficient at driving the motion of surrounding fluid.

Now consider the more realistic case in which the impeller size is less than the spacing between them, which is much less than the length of a microtubule, that is $a < d \ll L$. At a distance $r \gg d$, the velocity field will behave just as in the closed-packed case except appear to have a diminished impeller velocity. That is for $d \ll r \ll L$, the magnitude of the velocity $v(r) = v_0 f(a/d) g(r)$, where $g(r)$ contains all the distance dependence of the velocity field, and $f(a/d)$ is how the velocity scales with the ratio of a/d. In the limit where a/d is very small, the velocity between impellers will decay to zero. We recover the motion of isolated impellers in this case, where it is well known (e.g. Stokes' drag) that the velocity field is proportional to a. Therefore for small argument $x(= a/d)$, $f(x)$ is linear (in other words, the fluid velocity is proportional to a.) Using this general argument we conclude that, independent of the exact shape of the impellers, the flow velocity is reduced from the closed-packed case by a factor $\sim a/d$. The effect of the impellers only starts decreasing substantially at a distance of order the length of the microtubule, L, below which it should only have a weak logarithmic dependence. In other words, for a spherical region just enveloping a

microtubule, the fluid velocity is slowly varying and reduced from the kinesin motor velocity by a factor of order a/d. The above arguments suggest that only a low density of microtubules would be needed for cytoplasmic streaming. We will analyze the case of many microtubules below.

The above analysis only pertains to a single isolated microtubule. Because of the long range nature of the hydrodynamic interaction, the behavior of many microtubules will be quite different. Below we find that the consideration of many further enhances the streaming capablities of this system. To understand how this affects the above analysis, consider all space filled with an infinite forest of microtubules, all oriented in the same direction. First if we ignore the microtubules and just consider the spherical impellers, then if we move to a reference frame moving with the impeller velocity, the system is static and the velocity everywhere is zero. Therefore in the original reference frame, the fluid is also moving uniformly at the impeller velocity. This is not correct because we have ignored the hydrodynamic drag of the microtubules represented by the line going through the spheres in Fig. S1. To estimate their effect on the fluid velocity, we denote the drag coefficient on an impeller by b_I and that of a section of microtubule length d by b_M. Then we go to a reference frame velocity v such that the total force acting on the combined system of impellers and microtubules is zero, so that $b_I(v_0 - v) - b_M v = 0$, or $v = b_I v_0/(b_I + b_M)$. Because the net force acting on this system is zero in this frame, v is the velocity of the fluid far from the microtubules. Of course close to each microtubule, the velocity will differ from the value far away, but this will only affect points that are within a distance $a + d$ from the microtubule. If we assume conservatively, that the impellers are very thin cylindrical sheaths, fitting right over the microtubules, then this speed is $v_0 a/d$. If the hydrodynamic radius of the impellers is larger than such a model, then the velocity will be larger. The exact formula depends on the shape of the impellers. This argument assumes an infinite volume of microtubules but the corrections to this due to the finite nature of the system are not important for the estimates we are making.

3 Necessity of microtubule contact

The question of whether or not free floating microtubules with kinesin-driven impellers contribute to force generation for streaming is important. Our photobleaching tests demonstrate that there is a subcortical layer of microtubules that is stationary relative to the cortex, while subcortical cytoplasm streams past (Fig. 7 and Movie S7). In this case, the principle of Newton's third law dictates that the force on cytoplasmic fluid from plus-end directed kinesin-impeller movement is matched by an opposite force on microtubules that is transferred through the cortex to the surrounding tissues of the egg chamber and whatever it is attached too. Thus the impellers and fluid move while the microtubules do not, other than sinusoidal bending around their tethered minus ends. Could free microtubules deeper within the oocyte also drive flow? In this case, the force from kinesin-driven impellers on a microtubule will cause the microtubule to move with its minus-end leading, opposite the direction of the impellers. Because the force is equal in both directions, the motion imparted to cytoplasmic fluid must be equal in both directions. The result is that the microtubule will move one way, the impellers will move the other and, beyond very local displacements, the cytoplasm will not move.

From a more physical perspective, a free floating microtubule with kinesin moving on it will apply *zero* net force to the fluid. This is a simple consequence of Newton's third law, or equivalently, conservation of momentum. Consider a dumbell shaped machine with two spheres of different radii connected by a spring. Starting with the dumbell in a compressed state and then letting it go will impart equal and opposite forces on the two spheres, independent of their radii. Immersed in a viscous fluid, it is the total force that acts on a sphere that determines the velocity field of its surrounding fluid at large distances (see Eq. S-28). The fact that the small sphere travels a greater distance than the large one is irrelevant; they both impart equal and opposite forces to the fluid, so the net fluid movement at large distances is zero. This is analogous to the zero total charge on a dipolar object in electrostatics. Equal and opposite forces in a fluid imply dipolar fluid motion at large distances, which decays rapidly.

This does not contradict the fact that bacteria are able to swim: the force propelling the bacterium forward is countered by an equal and opposite force on the environment, leading to velocity fields that are dipolar at large distances, but still allowing motion of the bacterium due to local fluid displacement [19]. In the case analyzed above where kinesin is attached to microtubules, we have taken the microtubules to be static, and therefore momentum can be transfered between kinesin and microtubules, which will transfer the momentum through the oocyte cortex and membrane to the outside environment. When we consider the motion of microtubules, it is therefore important to have one end connected to the cortex to allow momentum transfer from the outside surroundings of the oocyte to the cytoplasm. Without such a microtubule connection to an external system, the motion of kinesin cannot lead to long range hydrodynamic motion of the fluid and will not lead to efficient cytoplasmic streaming by relatively few motor proteins. Contact with the cortex is therefore crucial, as it allows for transfer of force from the outside of the oocyte to the cytoplasm, enabling fast streaming of a large volume of cytoplasmic fluid to be powered by a much smaller volume of kinesin driven impellers.

4 Mathematical analysis of microtubule bending due to kinesin forces

During fast streaming, microtubules are largely aligned with each other and the local fluid motion, but they do exhibit chaotic wavelike bending motions. We begin with the equation for a single microtubule with an applied force tangent to the direction of the chain due to kinesin driving impellers toward the plus end. The position of the microtubule at arclength s and at time t is denoted $\mathbf{r}(s,t)$. As is usual at small scales, all inertial effects are negligible and the system is dominated by the drag coefficient per unit length ν,

$$\nu\frac{\partial \mathbf{r}}{\partial t} = -C\frac{\partial^4 \mathbf{r}}{\partial s^4} + \frac{\partial}{\partial s}(T(s)\frac{\partial \mathbf{r}}{\partial s}) - f_k\frac{\partial \mathbf{r}}{\partial s} + \nu v\hat{k}. \tag{S-1}$$

C denotes the elastic bending constant of the microtubule. The tension $T(s)$ enforces the inextensibility of microtubules which can be written as $|\partial \mathbf{r}/\partial s| = 1$. This is the three dimensional version of a two dimensional equation used to model rotating spiral patterns seen in motility assays [28] where we have added the extra term $\nu v\hat{k}$ discussed below.

Kinesin motors walking along the microtubule are assumed to be carrying cargoes that push on the cytoplasmic fluid that surrounds them. By Newton's third law, this force is matched by an equal and opposite force on the microtubule. Assuming a high density of kinesin, the effective force on the microtubule will be in the direction of the local tangent to $\mathbf{r}(s)$ which is $\partial \mathbf{r}/\partial s$. The coefficient f_k gives the strength of the force. Lastly we add a uniform flow field representing the velocity of the cytoplasm v in the vicinity of the microtubule which we take to be in the $\hat{k}$ direction.

We rescale to dimensionless variables

$$\sigma = s/\rho_0,\ \mathbf{U} = \mathbf{r}/\rho_0,\ \tau = t\omega_0,\ T' = T\rho_0^2/C,\ \text{and}\ h = \nu v/f_k \tag{S-2}$$

so that

$$\frac{\partial \mathbf{U}}{\partial \tau} = -\frac{\partial^4 \mathbf{U}}{\partial \sigma^4} + \frac{\partial}{\partial \sigma}(T'(\sigma)\frac{\partial \mathbf{U}}{\partial \sigma}) - \frac{\partial \mathbf{U}}{\partial \sigma} + h\hat{k}. \tag{S-3}$$

This requires that

$$\omega_0 = f_k/(\nu\rho_0),\ \text{and}\ \rho_0^3 = C/f_k. \tag{S-4}$$

ρ_0 and ω_0 are constants that make our new variables dimensionless.

We will consider solutions where the minus end is tethered to a point, say the origin, so that $\mathbf{r}(s = 0, t) = 0$ and is freely hinged at that point. The plus end is free. The total arclength of the microtubule is denoted by L. The general characteristic of all numerical solutions to Eq. S-1 is that for large s the solutions appear to be traveling waves. In fact, the form of solution becomes independent of L so in fact we could consider this problem in the limit $L \to \infty$. For example we find solutions that asymptotically become helical with a fixed path and radius for large s. Other solutions are planar and are periodic in s. In all these cases the solution has the form of a travelling wave that we analyze in detail below.

4.1 Steady State Travelling Wave Solutions

Now we look for steady state travelling wave solutions. First we clarify what this means; the whole microtubule should not be translating because the minus end, (far away from where the travelling wave solution is valid) is tethered. The position averaged over one period of a filament subunit, $\langle \mathbf{U} \rangle$, should be time independent. If the microtubule is stretched out in one particular direction, there should be a displacement $\mathbf{U}_d$ of the microtubule about a straight line solution, so we can look for solutions of the form

$$\mathbf{U}(\sigma, \tau) = \mathbf{U}_d(\sigma - v_d\tau) + \alpha\sigma\hat{k}. \tag{S-5}$$

The term $\mathbf{U}_d$ describes a transverse displacement waveform that travels along the backbone of the chain at velocity v_d, maintaining its shape. Here α is the extent to which the chain is extended in the direction of the fluild motion. Therefore we require

$$\frac{\partial \langle \mathbf{U}_d \rangle}{\partial \sigma} = 0 \tag{S-6}$$

where the average is taken over the argument $\sigma - v_d\tau$.

Since $\mathbf{U}_d$ is transverse, α sets the relation between σ and the z-axis ($\hat{k}$), such that $v_z = \alpha v_d$. If we choose $v_d = 1$ and in addition $\alpha = h$, we should obtain solutions that propagate along the fluid direction with the same unitless velocity as the fluid motion. Looking back to our original units, $v_d = 1$ corresponds to a wave propagating along the backbone of the chain at velocity f_k/ν (roughly the kinesin walking speed). Recall that h is the rescaled unitless velocity of the external flow field, so $\alpha = h$ is the condition that the traveling wave form should propagate along the axis aligned with the globally imposed fluid velocity at the same speed as the fluid. This will allow us to look for configurations that are stationary along that axis in the frame of the fluid.

Substituting Eq. S-5 into Eq. S-3 gives a left hand side of $-v_d\partial\mathbf{U}_d/\partial\sigma$ and a term of the form $-\partial\mathbf{U}_d/\partial\sigma$ on the right hand side, simplifying the equation to

$$\frac{\partial^4 \mathbf{U}}{\partial \sigma^4} + \frac{\partial}{\partial \sigma}(T'(\sigma)\frac{\partial \mathbf{U}}{\partial \sigma}) = 0. \tag{S-7}$$

We define $\mathbf{w} = \partial \mathbf{U}/\partial\sigma$ and note that the inextensibility requirement $|\partial \mathbf{r}/\partial s| = 1$ implies that $|\mathbf{w}| = 1$. We can write

$$\mathbf{w} = \frac{\partial \mathbf{U}_d}{\partial \sigma} + \alpha \hat{k} \tag{S-8}$$

Note that $\mathbf{w}(\sigma, \tau)$ depends only on $\sigma - \tau$. Because $\mathbf{w}$ is a function of only one variable $\xi \equiv \sigma - \tau$, we can integrate Eq. S-7 with respect to ξ obtaining

$$\frac{d^2\mathbf{w}}{d\xi^2} - T'(\sigma)\mathbf{w} = -g\hat{k}. \tag{S-9}$$

The integration constant on the right hand side $-g\hat{k}$ must lie in the $\hat{k}$ direction by symmetry. This is the same equation as that of the classical mechanics of a particle of unit mass, with position $\mathbf{w}$ travelling on the surface of a unit sphere under the influence of gravity, with the variable ξ being analogous to time. The term $-T'$ is a normal force that constrains the particle to stay on the sphere's surface.

From Eq. S-6 and Eq. S-8 we see that the motion is subject to the constraint

$$\langle \mathbf{w} \rangle = \alpha \hat{k} \tag{S-10}$$

The constant g and the initial conditions of the particle must be chosen so as to satisfy this constraint. There are an infinite number of solutions satisfying these conditions leading to different steady state solutions for the microtubule.

The spherical pendulum Eq. S-9 has been analyzed [S3] in detail. In general the orbits will not be closed, but we will relegate our discussion below to two cases where this is the case, circular motion in Eq. S-9, corresponding to helical conformations of a microtubule, and motion in the $x - z$ plane. The latter case is important when we introduce a hard wall, with the z axis being the direction of the global fluid field, and the solutions give shapes similar to cycloids.

4.2 Scale Invariant Family of Solutions

One important point to notice about the general structure of Eq. S-9 is its invariance under change of ξ, that is $\xi \to \lambda\xi$. A change in scale of λ does not modify the solution, because $T'(\xi)$ and g are

both constraints, and can therefore be chosen arbitrarily. So that if $\mathbf{w}(\xi)$ is a solution to Eq. S-9, so is $\mathbf{w}(\lambda\xi)$. Furthermore all solutions of this form will have the same $\langle\mathbf{w}\rangle$ and hence the same α. Note that a length scale shift of $\mathbf{w} = \mathbf{w}_0(\lambda\xi)$ corresponds to a displacement of $\mathbf{U} = (1/\lambda)\mathbf{U}_0(\lambda\xi)$, which changes scale because of the $1/\lambda$ prefactor in this expression. This means that for every steady state conformation of the microtubule, there exists a family of steady state solutions with identical shape but arbitrary size.

4.3 Circular Orbits

Circular orbits are solutions to Eq. S-9. Eq. S-10 requires that the vertical height of the orbit be at $w_z = \alpha$. Therefore the radius perpendicular to the global fluid velocity $\hat{k}$ (the w_x, w_y plane) is

$$w_\perp \equiv \sqrt{1-\alpha^2}. \tag{S-11}$$

It is first easiest to analyze this by direct analogy to the classical mechanical problem of a unit mass particle moving on a unit sphere (the spherical pendulum). If the height above the sphere is α, then application of Newton's laws gives that the tension must balance the force of gravity g and the centripetal acceleration $v^2/w_\perp$ giving

$$\frac{g}{v^2} \equiv \frac{\alpha}{1-\alpha^2} \tag{S-12}$$

Where v is not the real velocity of the microtubule but $|d\mathbf{w}_\perp/d\xi|$. This is the rate at which the tangent vector rotates in the $x-y$ plane (the plane perpendicular to the fluid motion). Because $|d\mathbf{U}_d/d\xi| = |\mathbf{w}_d| = r_c$ is a constant, $\mathbf{w}_d$ is a circle. Therefore according to Eq. S-5, this will give a helical conformation of the microtubule.

In the spherical pendulum analogy, the angular velocity of the particle is $\Omega_p = v/w_\perp$. The total arclength of the chain (in dimensionless units) of a single period of the chain is

$$S = \frac{2\pi R}{\sqrt{1-\alpha^2}} \tag{S-13}$$

and $S\Omega_p = 2\pi$ so that $S = 2\pi/\Omega_p = w_\perp/v$. Comparing this with Eq. S-13 we obtain

$$R = \frac{w_\perp}{v}\sqrt{1-\alpha^2}. \tag{S-14}$$

Using Eq. S-11 this gives

$$R = \frac{1-\alpha^2}{|\frac{dw_\perp}{d\xi}|} = \frac{1-\alpha^2}{v} \tag{S-15}$$

Because g is a free parameter, v can be any positive number and therefore Eq. S-15 implies that the radius of the helix can be arbitrary.

Because the velocity of this travelling wave is unity, the spatial and temporal periodicities are equal. Therefore the period of rotation of the helix P' is equal to S in Eq. S-13, in the dimensionless units that we are using. Therefore the relationship between the period and the pitch is

$$P' = \frac{2\pi R}{\sqrt{1-\alpha^2}} \tag{S-16}$$

In terms of our original units the period is

$$P = \frac{2\pi R\nu}{f_k\sqrt{1-\alpha^2}} \tag{S-17}$$

4.4 Two Dimensional Solutions

As we will see in Sec. 4.5, the presence of a wall often causes conformations to become flat, that is two dimensional. Therefore it is of interest to analyze this case. We consider orbits in the $x-z$ plane. This corresponds to a pendulum swinging around vertically through the bottom of the sphere. This is a standard introductory mechanics problem. Letting θ denote the angle with respect to the $-\hat{k}$ direction,

$$\ddot{\theta} = -g\sin\theta \tag{S-18}$$

where the dots that normally represent a time derivative are really derivatives with respect to ξ. Low energy solutions where the total energy E is less than g give θ oscillating between two bounds. In this case the curve for the microtubule will look sinusoidal. Beyond the separatrix where $E > g$,

θ will increase without bound. This gives rise to microtubule conformations that look close to prolate cycloids. In other words, the microtubule forms a travelling wave that periodically loops backwards (Fig. S2).

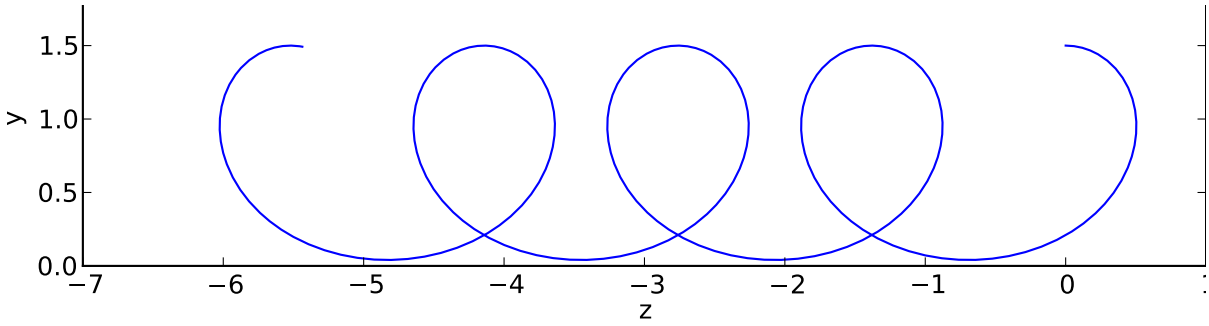

Figure S2: A two dimensional travelling wave solution for a microtubule that looks close to a prolate cycloid but differs from it in functional form.

Small values of $|\alpha|$ correspond to low values of g/E. In this case, the particle spends almost equal times at all points on the circle giving a small value of $\langle w \rangle = \alpha$. As g/E increases to 1, α increases and the loops become tighter; a situation that is very costly energetically. However this is not the only solution to these equations for a fixed value of α. If instead we consider solutions with $E < g$, then large g/E corresponds to small oscillations of $\mathbf{w}$ about $-\hat{k}$. In this case, $|\alpha|$ is close to 1 and the curve has no tight loops. The shape of the microtubule is close to a sine wave.

To obtain the relationship between $G \equiv g/E$ and α we use conservation of energy to obtain the period,

$$\dot{\theta} = \sqrt{2E(1 + G\cos\theta)} \tag{S-19}$$

The time average of $\mathbf{w}$ in the $\hat{k}$ direction is

$$\langle \cos\theta \rangle = \frac{\int_0^\pi \frac{\cos\theta}{\sqrt{1+G\cos\theta)}} d\theta}{\int_0^\pi \frac{1}{\sqrt{1+G\cos\theta)}} d\theta} \tag{S-20}$$

This can be expressed in terms of elliptic integrals as

$$\langle \cos\theta \rangle = \frac{1}{G}(1 - (1+G)\frac{\mathsf{E}(2G/(1+G))}{\mathsf{K}(2G/(1+G))}) \tag{S-21}$$

Where E and K are the complete Elliptic integrals of the first and second kind respectively. For bounded orbits, below the separatrix, the corresponding expression can be calculated giving

$$\langle \cos\theta \rangle = -2\frac{\mathsf{E}(\frac{e+1}{2})}{\mathsf{K}(\frac{e+1}{2})}) + 1 \tag{S-22}$$

A plot of the $\alpha = \langle \cos\theta \rangle$ versus $1/G = E/g$ is shown in Fig. S3 using these two expressions. $\alpha \to 0$ in the limit as $G \to 0$. Note that there are two possible values of E/g corresponding to one value of positive α.

The case of $\alpha = 0$ corresponds to the case of circular orbits discussed in Sec. 4.3. The cytoplasmic streaming velocity is $\propto h$ (see Eq. S-3). When $h = 0$, we have shown that the solutions are circular. If h is now made very small, we expect that the solution will only be slightly perturbed from circular solutions. This corresponds to a small value of g/E. Therefore the value of G that is chosen for small enough h should correspond to the larger value of $1/G$ shown in Fig. S3. This corresponds to almost circular loops shifting slightly forward after every turn. As h increases, the loops become tighter giving rise to a high elastic bending energy. At some point therefore, we expect a transition to another state. In fact, simulations discussed in Sec. 4.6 show that near a flat surface, the microtubule transitions out of the plane to a helical shape at $h \approx .385$ for 128 links in a chain. For still larger h, the microtubule becomes flat again looking close to sinusoidal.

4.5 Numerical Implementation of the Full Solutions

By comparing the steady state solutions found above for large arclength s and time t, we will see that these solutions are physically realistic ones to consider. As we will see, the full equations of motions go to solutions of this type. However this is not a complete description of the problem, because of these solutions a particular one is selected from a whole family of solutions. The same behavior occurs in other problems in pattern selection such as dendritic growth [S4, S5].

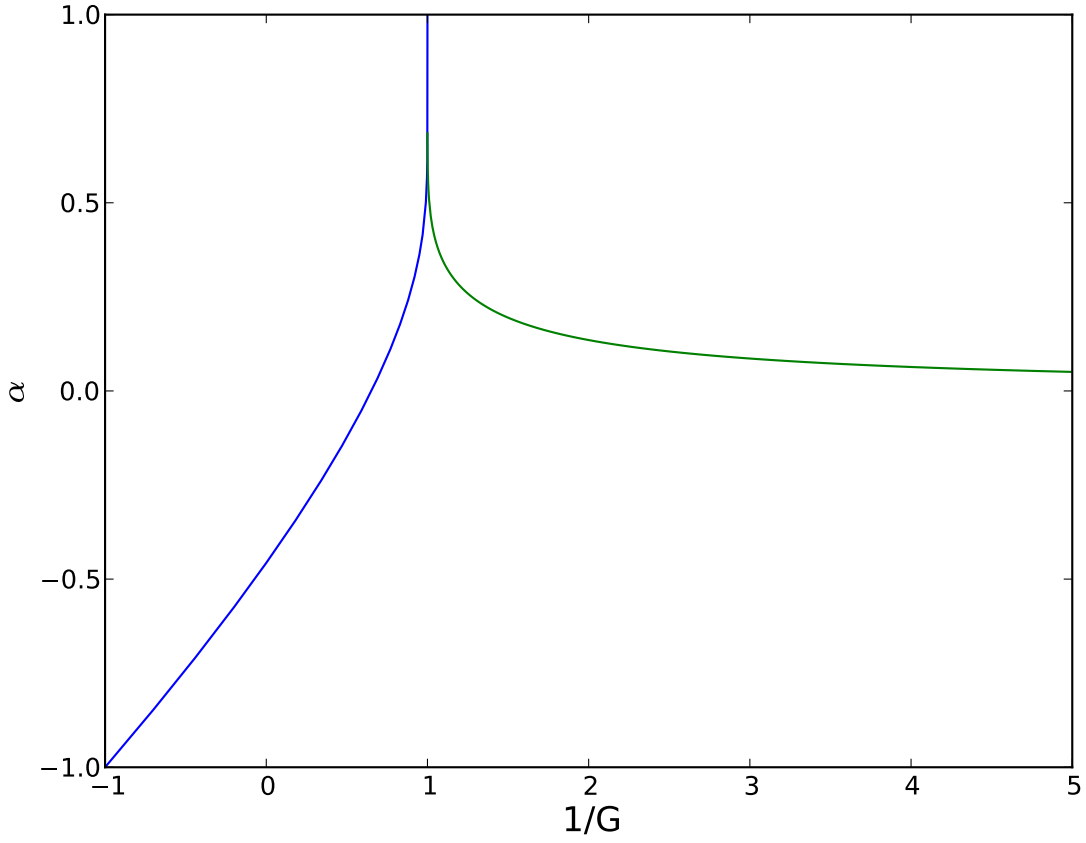

Figure S3: A plot of the value of α, the wave propagation velocity, as a function of $1/G$, which is the energy of the analogous spherical pendulum.

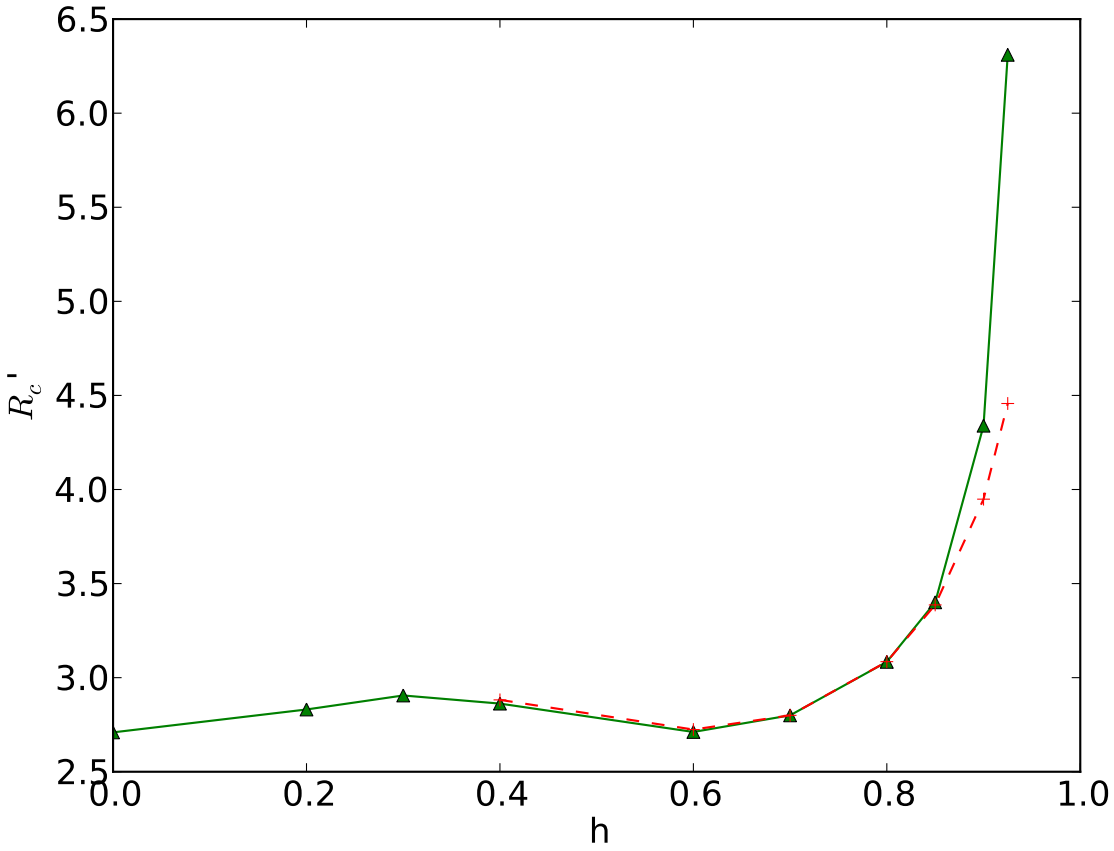

Figure S4: The rescaled radius of curvature for the helical configuration, R_c/ρ_0, versus the rescaled fluid velocity field $h = \alpha$. The green triangles are for 64 link chains, the red + symbols are for chains of 128 links.

4.6 Comparison With Simulation

Eq. S-1 was analyzed numerically using a method similar to that used in the context of gel electrophoresis [S6, S7]. Link length drift was handled using a similar procedure to that implemented for chains with inertia [S8] One end was constrained to have coordinates at the origin, while the

other was free.

A Runge Kutta time step was 0.001, with the elastic bending coefficient $C = 20$, the kinesin force magnitude $f_k = 2$ and simulations were performed with $N = 64$ or $N = 128$ links, as will be noted below. The units are such that the distance between links is set to unity, and the friction coefficient ν, which determines the units of time, is also set to 1.

We first consider the case of a microtubule with no wall or other external forces aside from the external velocity field. As a function of the rescaled external velocity field h, the radius of curvature and period were calculated once the system had reached steady state. Using rescaled variables as defined by Eqs. S-2 and S-4 we can write the dimensionless radius of curvature as $R_c' = R_c/\rho_0$, and the dimensionless period as $P' = \omega P$. The radius of curvature was calculated at the middle of the chain to reduce finite size effects. The results are shown in Figs. S4 and S5. The data for R_c, Fig. S4 using 64 links, is very close to those of 128 links except for the highest h values. The data for the period, Fig. S5(a) show good agreement for both chain sizes at all values of h studied.

We now test the analytic predictions that we made relating the period to the radius of the helix and α given by Eq. S-16, and our conclusion that $\alpha = h$. The relationship between the radius of curvature R_c and the radius R of the helix is readily calculated to be $R = R_c(1 - \alpha^2)$. Therefore Eq. S-16 gives

$$P' = 2\pi R_c' \sqrt{1 - \alpha^2} \tag{S-23}$$

With this prediction, and using the data for R_c in Fig. S4, we can independently calculate P' for 64 link chains. We can only do this where finite size effects are not important and therefore omit the highest two h values from this analysis. The data, Fig. S5(b), show excellent agreement to within the differences expected by finite size effects. This corroborates our analytical analysis of steady state solutions.

The case of $h = \alpha = 0$ displayed in Fig. S4 can be written in terms of the original dimensional variables of Eq. S-1 using Eq. S-4

$$\nu R\omega / f_k = 1. \tag{S-24}$$

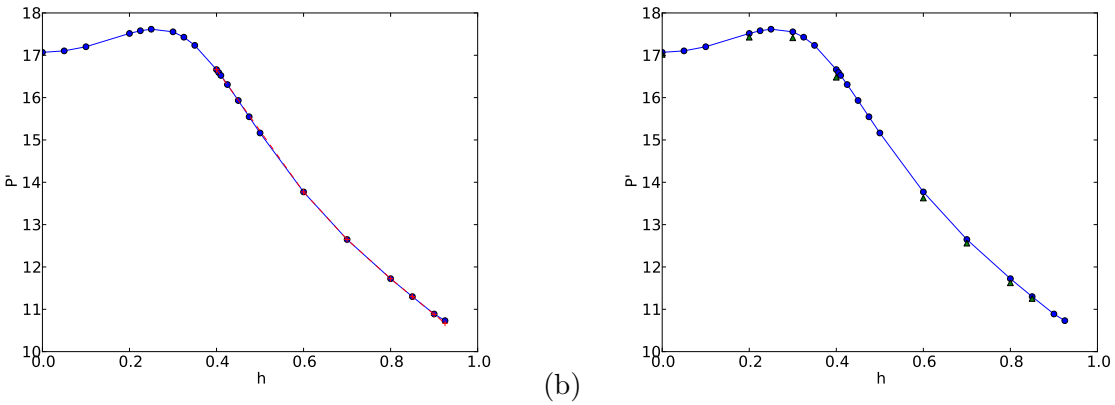

Figure S5: (a)The rescaled period $P' = P\omega$ versus the rescaled velocity field $h = \alpha$. The blue circles are for 64 link chains, the red + symbols are for chains of 128 links. Here the period is measured directly by timing repeated motion. The line is a guide for the eye. (b) The rescaled period $P' = P\omega$ versus the rescaled velocity field $h = \alpha$ calculated by using Eq. S-23 and data on the radius of the helix versus h shown in Fig. S4. The result is shown by the green triangles. The blue circles are the same data shown in Fig. S5(a) by directly measuring the period, which shows good agreement with the numbers produced by using Eq. S-23. Again the line is a guide for the eye.

And using our numeric solutions we can obtain.

$$R_c = (C/(\beta f_k))^{1/3}. \tag{S-25}$$

From the numerical solution, this gives $\beta = 0.05 \pm 0.0005$. This is useful in analyzing experimental data, as R_c is nearly constant for $h < 0.7$.

Next we consider the presence of a wall. We introduced a force representing a wall in the $y - z$ plane of the form

$$\mathbf{f}_w = \frac{x^2}{(x+1)^2}\hat{i} \tag{S-26}$$

which is only present for $x < 0$. The force is singular at $x = -1$ preventing the chain from crossing that plane. The period as a function of h is shown in Fig. S6 for $C = 20$ and chains with 128 links.

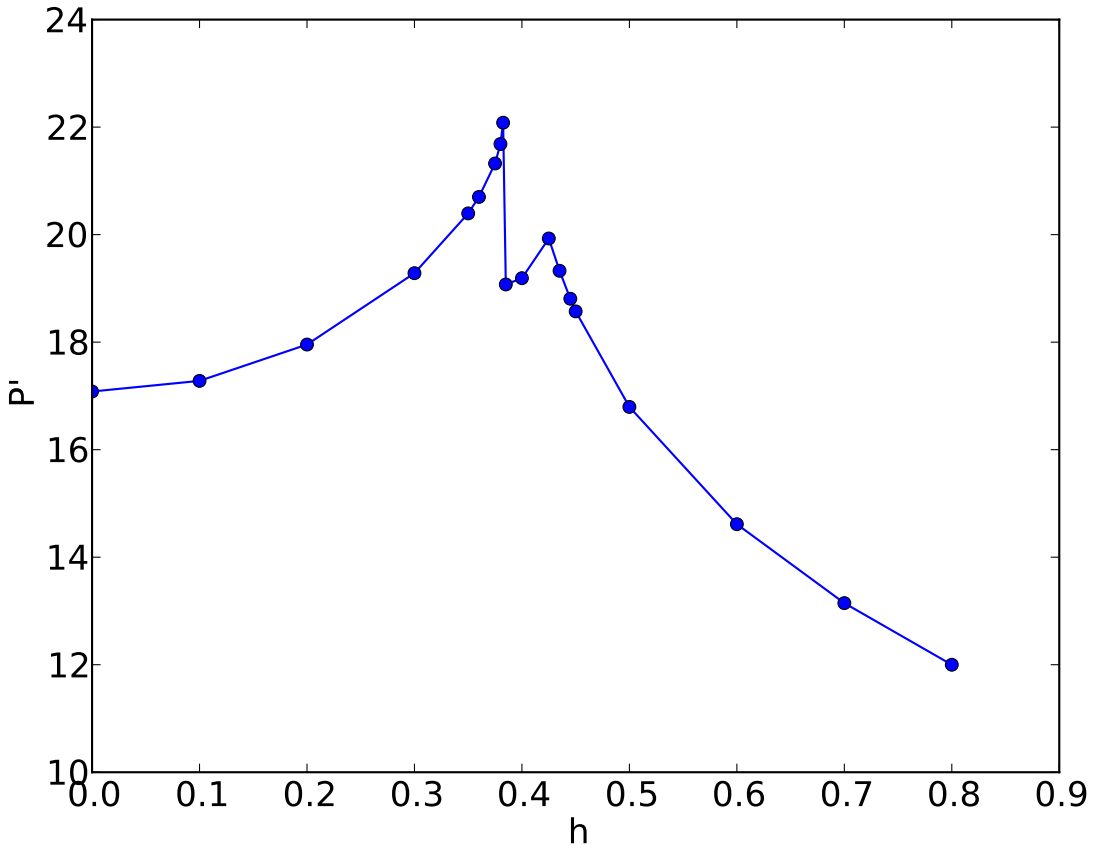

Figure S6: The rescaled period $P' = P\omega$ versus the rescaled velocity field $h = \alpha$ for chains of 128 links.

For small values of h, the period does not vary much. The shapes obtained are flat and appear to be the same as those found in Sec. 4.4. However there is non-analytic behavior at $h \approx 0.385$

corresponding to a transition to flattened helical waves. Then at $h \approx 0.425$ the solution becomes almost completely flat and showing waves that look closer to sine waves, corresponding to the flat sinusoidal-like solutions studied in Sec. 4.4.

We now consider the dependence of period and curvature on the length of chains L. Our analytical solutions have been in the limit that the chain length $L \to \infty$. For finite length chains, we expect corrections to this behavior. In this case we consider $h = 0$ and study how the rotating spiral wave solutions vary with increasing length. Fig. S7(a) shows the dependence of the radius of curvature measured halfway along the arclength, as a function of chain length. As usual, the rescaled dimensionless variables, see Eqs. S-2 and S-4 have been used. The curve shows a non-monotonic dependence on L that levels off at $L \approx 20$. Fig. S7(b) shows that the rescaled period is slightly non-monotonic as well but decreases to a constant value at $L \approx 15$.

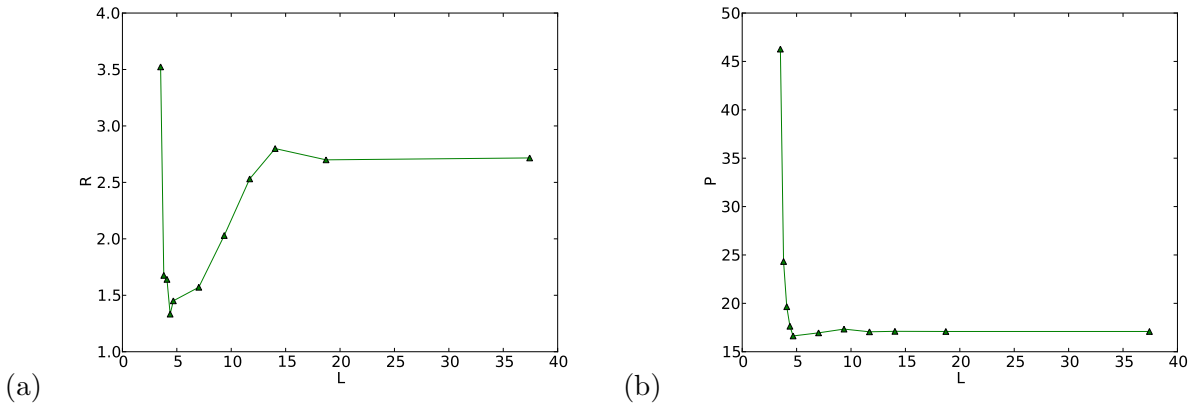

Figure S7: (a) The rescaled radius of curvature measured at the middle link of a chain versus the rescaled chain length in steady state for $h = 0$. (b) The rescaled period versus the rescaled chain length in steady state for $h = 0$.

Note that in Fig. S7(b) the period diverges for finite $L \approx 3$. Below this point, the solution is a static straight line. This is similar to the usual buckling transition for a finite length elastic rod [S9]. Thus the microtubule needs to be sufficiently long to undergo the dynamical instability

analyzed here.

4.6.1 Selection of Scale

As noted in Sec. 4.2, there exists a continuous family of steady state solutions because if $\mathbf{w}(\xi)$ is a solution, then so is $\mathbf{w}(\lambda\xi)$ for arbitrary λ. The general way that a particular value of λ is selected is likely to be due to the same mechanism as in other pattern formation problems [S4, S5]. The travelling wave solutions ignore the boundary conditions at the ends $s = 0$ and $s = L$. Far from those ends, we have found a continuous family of solutions. However these solutions become invalid close to the ends. The travelling wave solutions are only valid in the limit of $0 << s << L$. The full solution must match to one of these travelling solutions in that region but will differ greatly near the ends.

As an example, consider the circular solutions of Sec. 4.3 with $h = \alpha = v = 0$. There the steady state solution is a rotating circle wrapped around on itself of *arbitrary radius* R. However near the end $s = 0$, the solution goes into the circle's center. Similarly it deviates from a circle at $s = L$. In analogy with other pattern growth problems such as the "Geometric Model" [S4], where the mathematics have been analyzed in detail, we expect that the boundary conditions imposed on the ends, will only be satisfied for certain values of R. If there is more than one allowed value of R, the value picked out will be the most stable of these. In the Geometric Model the form of the equations is much simpler, making it possible to understand the overall structure of the problem more easily. In the present case, a precise understanding of the numerical results will be the subject of future research.

5 Fluid Mediated Polymer Interactions

After the foregoing analysis of the dynamics of individual polymers in an externally imposed flow field, we now investigate how such a flow field could actually be generated internally by kinesin forces acting on a large group of microtubules. To produce a global flow field in the fluid, we need a

large number of microtubules all aligned and contributing to the driving of the field in a correlated manner. In addition to investigating steady state values, the behavior with small kinesin forces could determine criteria under which spontaneous global velocity field formation could occur. To do these types of calculations, a more detailed view of the interaction between elements in the system needs to be taken.

5.1 Introduction to the Oseen Tensor

Since streaming occurs in a low Reynolds number regime, the motion of the fluid is described by the simplified Stokes equations:

$$\begin{aligned} \nabla p &= \mu \nabla^2 \mathbf{u} + \mathbf{f} \\ \nabla \cdot \mathbf{u} &= 0 \end{aligned} \tag{S-27}$$

The linearity of the Stokes equations allows for solutions to be obtained via a Green's Function, such that for a continuous force density $\mathbf{f}(\mathbf{r})$,

$$\begin{aligned} \mathbf{u}(\mathbf{r}) &= \int \mathbf{f}(\mathbf{r}') \cdot \mathbf{J}(\mathbf{r} - \mathbf{r}') d\mathbf{r}' \\ p(\mathbf{r}) &= \int \tfrac{\mathbf{f}(\mathbf{r}') \cdot (\mathbf{r} - \mathbf{r}')}{4\pi |\mathbf{r} - \mathbf{r}'|^3} d\mathbf{r}' \end{aligned} \tag{S-28}$$

Where

$$\mathbf{J}(\mathbf{r}) = \frac{1}{8\pi\mu} \left(\frac{I}{|\mathbf{r}|} + \frac{\mathbf{r}\mathbf{r}^T}{|\mathbf{r}^3|} \right) \tag{S-29}$$

is a second rank tensor field known as the Oseen Tensor. The Oseen tensor has had great success in describing how small or thin objects interact in fluid, as well as the self interaction of polymers. When used to describe the effect of applying force to a very small sphere of radius a, the Oseen tensor has higher order corrections in $a/\mathbf{r}$, where $\mathbf{r}$ is the distance from the sphere, but these begin at $(a/\mathbf{r})^3$ and should not play a significant role in cross polymer interactions. Of particular interest is its use in modeling polymers as a long chain of beads, which will lend itself well to numerical simulation.

5.2 Model for Hydrodynamic Interactions

For this multi-filament model, we are going to use the same structure for the microtubule as for the solitary case. This models the microtubule as a chain of beads with some tension T and stiffness parameter C. The equation of motion for each microtubule in the array is modified now by the inclusion of the Oseen interaction tensor. Each microtubule and its kinesin-driven impellers are in direct contact with the fluid and at the interface the velocity of the fluid must match the velocity of the objects suspended in it. This means that any force exerted on the objects will also be transmitted to the fluid locally. These forces form the force density used in the Oseen tensor to determine the fluid velocity in all of space, which will also determine the motion of the microtubule and impeller system.

This is a bit more complex than simply adding the tensor to the previous equation of motion, as the interaction tensor needs to include the forces of all objects moving in the fluid. Previously, we simply included the kinesin as a force tangent to the backbone of the microtubule, and while that is still going to be our model, we now need to include consideration for the reaction force produced against the impeller, as this will be transmitted back to the microtubule by the long range hydrodynamic forces.

In order to determine the effect that this extra force density will have on the dynamics, we need to be more explicit with the configuration of the impellers. Consider the impellers of largest dimension q to be attached to the microtubule by kinesin motors with no side being preferred at a characteristic distance a with, as in the single microtubule consideration, $a < q \ll L$, with L again being the microtubule length. We can consider this to form a uniform density of impellers around the microtubule, and the kinesin motors cause the impeller and the microtubule to move relative to each other with a fixed velocity in the direction of the tangent of the microtubule backbone.

The fluid velocity field can now be computed by applying the Oseen tensor and integrating over the force densities present in the system. The forces acting on the microtubule can be integrated by integrating over the backbone of the chain. The forces acting on the impellers can be computed

by integrating over a cylindrical sheath around the microtubule, giving us

$$\mathbf{u}(\mathbf{r}) = \int \left[\mathbf{J}(\mathbf{r} - \mathbf{r}'(s))[-C\frac{\partial^4 \mathbf{r}'}{\partial s^4} + \frac{\partial}{\partial s}(T(s)\frac{\partial \mathbf{r}'}{\partial s}) - \mathbf{f_k}] + \int \mathbf{J}(\mathbf{r} - \mathbf{r}'(s) + \mathbf{a}(s))\frac{\mathbf{f_k}}{2\pi|\mathbf{a}|}\frac{\partial \mathbf{r}'}{\partial s} d\hat{\mathbf{a}} \right] ds \tag{S-30}$$

where $\mathbf{u}$ is the fluid velocity and $\mathbf{a}$ is a vector pointing radially outward from the microtubule axis to the impeller location. Recall that C, $T(s)$, and $\mathbf{f_k}$ are the microtubule stiffness parameter, microtubule tension, and kinesin walk force respectively. Because the microtubule system is in contact with the fluid, the motion of the microtubule will follow that of the fluid along the backbone locations. However, due to the long range of the hydrodynamic interaction, the system can now be far more sensitive to the overall configuration, which could potentially lead to more complex steady state solutions than we found for the non interacting single microtubule solutions of Sec. 4.

There are three primary generators of force; backbone stiffness, a gradient in backbone tension, and the kinesin motors. The first two force densities can be computed entirely from the microtubule configuration, and these values can then be used as inputs to the Oseen tensor. The force due to the kinesin coupling and walking is difficult to analyze, however, we will show that it has negligible effect on the long range fluid motion. We will see that this somewhat paradoxical situation still leads to long range fluid flow, as we will discuss below.

5.3 Kinesin Quadrupole

In order for the kinesin to drag the impeller along, it must push against the microtubule, so the force moving the impeller through the fluid has a corresponding opposite force on the microtubule by Newton's third law. Both of these forces are then transmitted to the fluid, so it is reasonable to try to express these forces as some multipole expansion in a small parameter. The microtubules have a significant stiffness which leads to a characteristic buckling length as described in Eq. S-25, which sets a size scale for features of the microtubule motion. Compared to this size scale, the impellers are very small, and bound very tightly to the microtubule backbone. In addition to this,

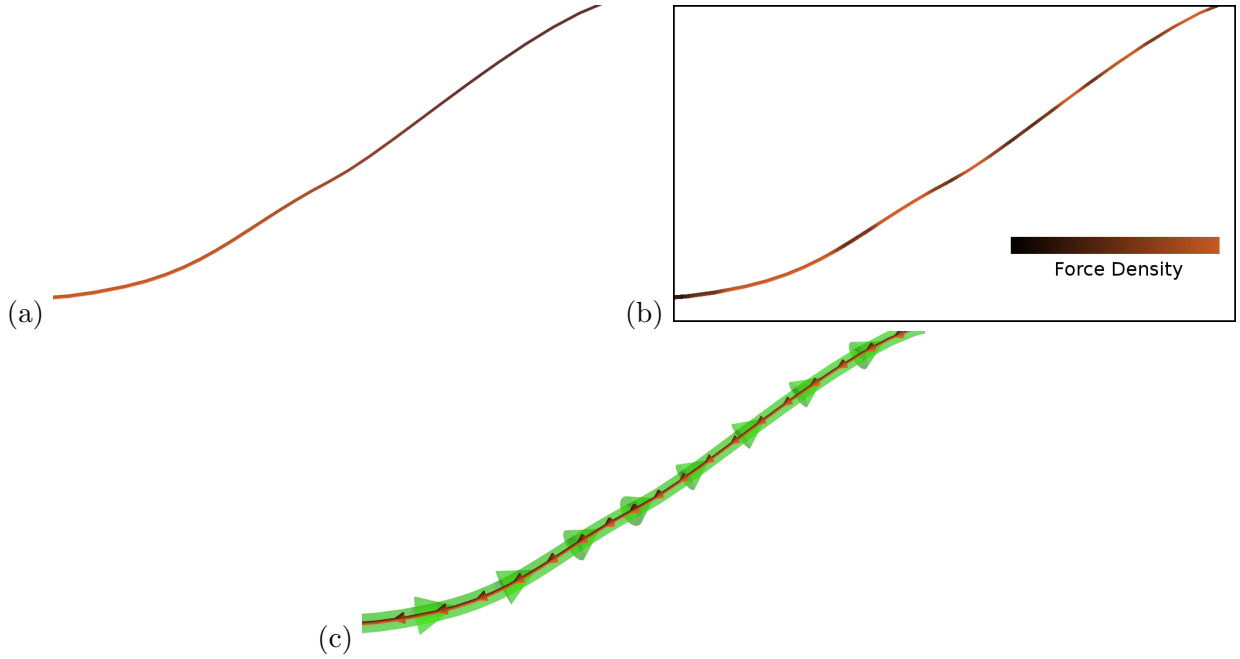

Figure S8: (a) A gradient in tension creates a force density along the axis of the microtubule backbone. This is determined by the microtubule configuration. (b) The microtubule curvature creates a force density (black low and red high) that acts on the fluid. This is also determined by the microtubule configuration. (c) The kinesin motors act on both the microtubule (red arrows) and the impellers (green arrows), applying forces that bind them together and drive the impellers along the microtubule. Both of these force densities are transmitted to the fluid. These force densities arise due to a local coupling, and therefore are related by Newton's third law.

we assume that the impellers are attached to the microtubule in a cylindrically symmetric fashion. This leads to a small scale force distribution that looks like a classic quadrupole configuration, as shown in Fig. S9.

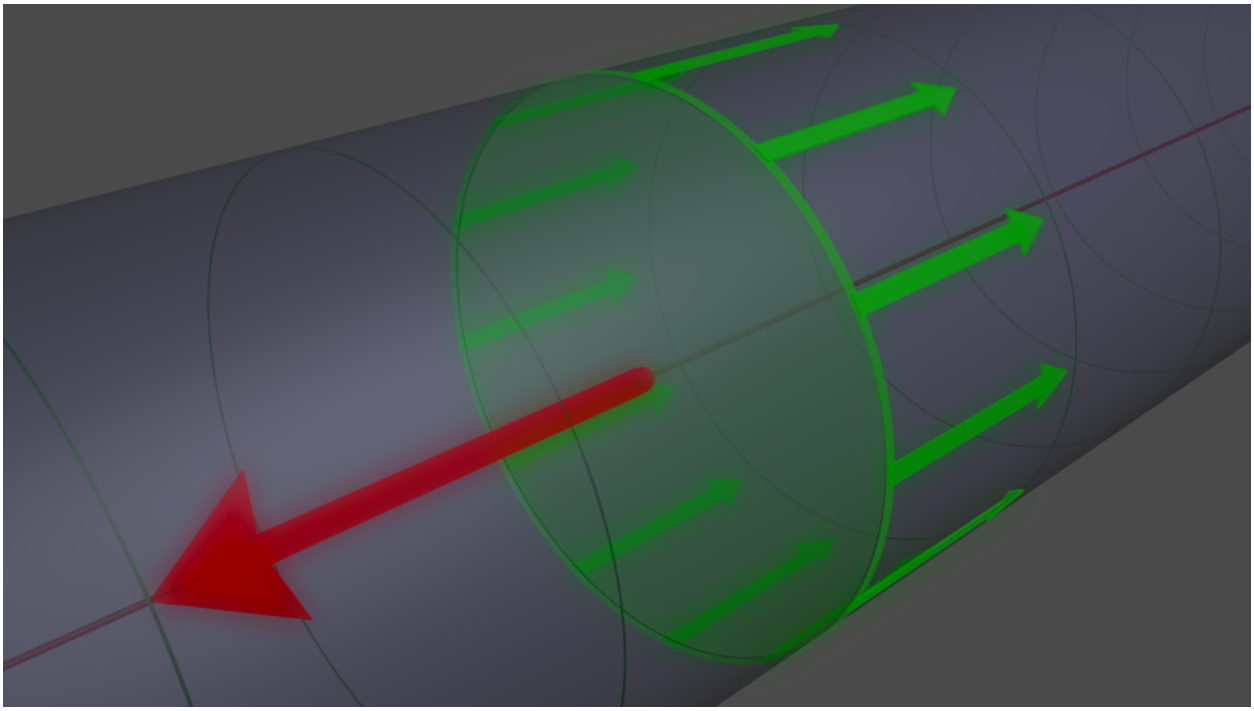

Figure S9: At a given location along the microtubule (maroon line), the forces generated by the kinesin motors push on the microtubule and the impellers in opposite directions. This force density has a cylindrically symmetric shape, which contributes to a rapid falloff in the effect it has on the fluid.

We next investigate the contribution to the fluid velocity field from a small segment of the microtubule impeller system. For convenience, place the segment at the origin, and calculate the fluid motion at position $\mathbf{r}$. The kinesin motors apply force between the microtubule and impellers in two ways. They walk along the axis of the microtubule producing significant force along the

axis, and they also hold the impellers onto the microtubule, creating a rigid link force radially. A key feature of the nature of these forces is symmetry of inversion through the center axis.

We can now write down the fluid response due to this force density.

$$\delta\mathbf{u}(\mathbf{r}) = \frac{1}{8\pi\mu}\int \frac{\mathbf{f}}{|\mathbf{r}+\mathbf{a}|} + \frac{(\mathbf{r}+\mathbf{a})((\mathbf{r}+\mathbf{a})\cdot\mathbf{f})}{|\mathbf{r}+\mathbf{a}|^3}d\hat{\mathbf{a}} - \frac{\mathbf{F}}{|\mathbf{r}|} - \frac{\mathbf{r}(\mathbf{r}\cdot\mathbf{F})}{|\mathbf{r}|^3} \tag{S-31}$$

Where $\delta\mathbf{u}(\mathbf{r})$ is the contribution to the fluid velocity at position $\mathbf{r}$ from a differential segment of the microtubule impeller system, a is the vector pointing from the center of the microtubule to a point in the impeller sheath, F is the linear force density on the microtubule backbone produced by the kinesin walkers, and f is an area force density of the force needed to drag the impeller sheath through the fluid. Because the kinesin binds the microtubule and the impeller together, Newton's Third Law dictates that the linear force density along the backbone needs to be equal and opposite for the impeller microtubule pair. This gives us that integrating f around the full circle must give the same value as F. Due to the small size of the kinesin molecule, for long range interaction on the order of the length of the microtubule, or even characteristic curvatures of the microtubule, we should have $a << r$, where a and r are the magnitudes of $\mathbf{a}$ and $\mathbf{r}$ respectively. We can pull out a factor of r to obtain these expressions in terms of a unit-less small parameter $\epsilon = a/r$.

$$\int \frac{\mathbf{f}}{|\mathbf{r}+\mathbf{a}|} + \frac{\mathbf{r}(\mathbf{r}\cdot\mathbf{f})}{|\mathbf{r}+\mathbf{a}|^3}d\mathbf{a} \tag{S-32}$$

Becomes

$$\int \frac{\mathbf{f}}{r|\hat{\mathbf{r}}+\epsilon\hat{\mathbf{a}}|} + \frac{(\hat{\mathbf{r}}+\epsilon\hat{\mathbf{a}})((\hat{\mathbf{r}}+\epsilon\hat{\mathbf{a}})\cdot\mathbf{f})}{r|(\hat{\mathbf{r}}+\epsilon\hat{\mathbf{a}})|^3}d\hat{\mathbf{a}} \tag{S-33}$$

Apart from a global factor of $1/r$, only the directions of $\mathbf{r}$ and $\mathbf{a}$ remain, with all of the distance scaling being absorbed into the small parameter ϵ. We can now expand the expression to find what the leading order contribution to the fluid velocity field will be. The zeroth order term reduces simply to

$$\delta\mathbf{u_0}(\mathbf{r}) = \int \frac{\mathbf{f}}{r|\hat{\mathbf{r}}|} + \frac{(\hat{\mathbf{r}})(\hat{\mathbf{r}}\cdot\mathbf{f})}{r|(\hat{\mathbf{r}})|^3}d\hat{\mathbf{a}} - \frac{\mathbf{F}}{|\mathbf{r}|} - \frac{\mathbf{r}(\mathbf{r}\cdot\mathbf{F})}{|\mathbf{r}|^3} \tag{S-34}$$

Which will vanish due to the requirement of Newton's Third Law. The first order term in ϵ requires a bit more work, but is still a straightforward derivative. We first need to expand the magnitudes

in terms of a square root as follows,

$$\delta\mathbf{u}(\mathbf{r}) = \frac{1}{r}\int \mathbf{f}[(\hat{\mathbf{r}}+\epsilon\hat{\mathbf{a}})^2]^{-1/2}d\hat{\mathbf{a}} + (\hat{\mathbf{r}}+\epsilon\hat{\mathbf{a}})(\hat{\mathbf{r}}+\epsilon\hat{\mathbf{a}})\cdot\mathbf{f}[(\hat{\mathbf{r}}+\epsilon\hat{\mathbf{a}})^2]^{-3/2}d\mathbf{a} - \frac{\mathbf{F}}{|\mathbf{r}|} - \frac{\mathbf{r}(\mathbf{r}\cdot\mathbf{F})}{|\mathbf{r}|^3} \tag{S-35}$$

$$\begin{aligned}
\tfrac{d}{d\epsilon}\delta\mathbf{u}(\mathbf{r}) &= \tfrac{1}{r}\textstyle\int -\mathbf{f}[(\hat{\mathbf{r}}+\epsilon\hat{\mathbf{a}})^2]^{-3/2}(\hat{\mathbf{r}}+\epsilon\hat{\mathbf{a}})\cdot\hat{\mathbf{a}} \\
&+ \hat{\mathbf{a}}(\hat{\mathbf{r}}+\epsilon\hat{\mathbf{a}})\cdot\mathbf{f}[(\hat{\mathbf{r}}+\epsilon\hat{\mathbf{a}})^2]^{-3/2} \\
&+ (\hat{\mathbf{r}}+\epsilon\hat{\mathbf{a}})(\hat{\mathbf{a}}\cdot\mathbf{f})[(\hat{\mathbf{r}}+\epsilon\hat{\mathbf{a}})^2]^{-3/2} \\
&- 3((\hat{\mathbf{r}}+\epsilon\hat{\mathbf{a}})(\hat{\mathbf{r}}+\epsilon\hat{\mathbf{a}})\cdot\mathbf{f}[(\hat{\mathbf{r}}+\epsilon\hat{\mathbf{a}})^2]^{-5/2}(\hat{\mathbf{r}}+\epsilon\hat{\mathbf{a}})\cdot\hat{\mathbf{a}}
\end{aligned} \tag{S-36}$$

$$\begin{aligned}
\lim_{\epsilon\to 0}\tfrac{d}{d\epsilon}\delta\mathbf{u}(\mathbf{r}) &= \tfrac{1}{r}\textstyle\int -\mathbf{f}[(\hat{\mathbf{r}})^{\mathbf{2}}]^{-\mathbf{3/2}}(\hat{\mathbf{r}})\cdot\hat{\mathbf{a}} \\
&+ \hat{\mathbf{a}}(\hat{\mathbf{r}})\cdot\mathbf{f}[(\hat{\mathbf{r}})^2]^{-3/2} \\
&+ (\hat{\mathbf{r}})(\hat{\mathbf{a}}\cdot\mathbf{f})[(\hat{\mathbf{r}})^2]^{-3/2} \\
&- 3((\hat{\mathbf{r}})(\hat{\mathbf{r}})\cdot\mathbf{f}[(\hat{\mathbf{r}})^2]^{-5/2}(\hat{\mathbf{r}})\cdot\hat{\mathbf{a}}
\end{aligned} \tag{S-37}$$

As we can see, each term in the integrand is an odd function of $\hat{a}$, and the integral is around the whole circle, so this vanishes. This means that the leading order term from the kinesin coupling force density is going to be suppressed by two factors of the small parameter ϵ. In comparison, the tension can be decomposed into equal and opposite pairs between adjacent segments of the microtubule. However, we will find that they are not able to form a quadrupole like the kinesin forces do. The separation between the two opposing forces is axial, and lacks the mirror symmetry needed to form the quadrupole. This means that it would give rise to a dipolar term. And even in the case of the dipolar term, the corresponding small parameter needed to form the multipole cancellation is directly tied to the characteristic length scale of the microtubule curvature; indeed, the curvature is defined by these forces. So not only would it be a chain of dipoles, the density of those dipoles would need to diverge in the limit of small separation between the opposing forces. If we instead sum the forces on each individual segment, we are left with the simple linear force density of the gradient of the tension. This gradient is expected to be nonzero due to the tethering of the microtubule minus-end. A nonzero linear force density along the axis of the microtubule would apply directly through the Oseen tensor with no cancellation, and thus fall off as $\mathbf{r}^{-1}$, where

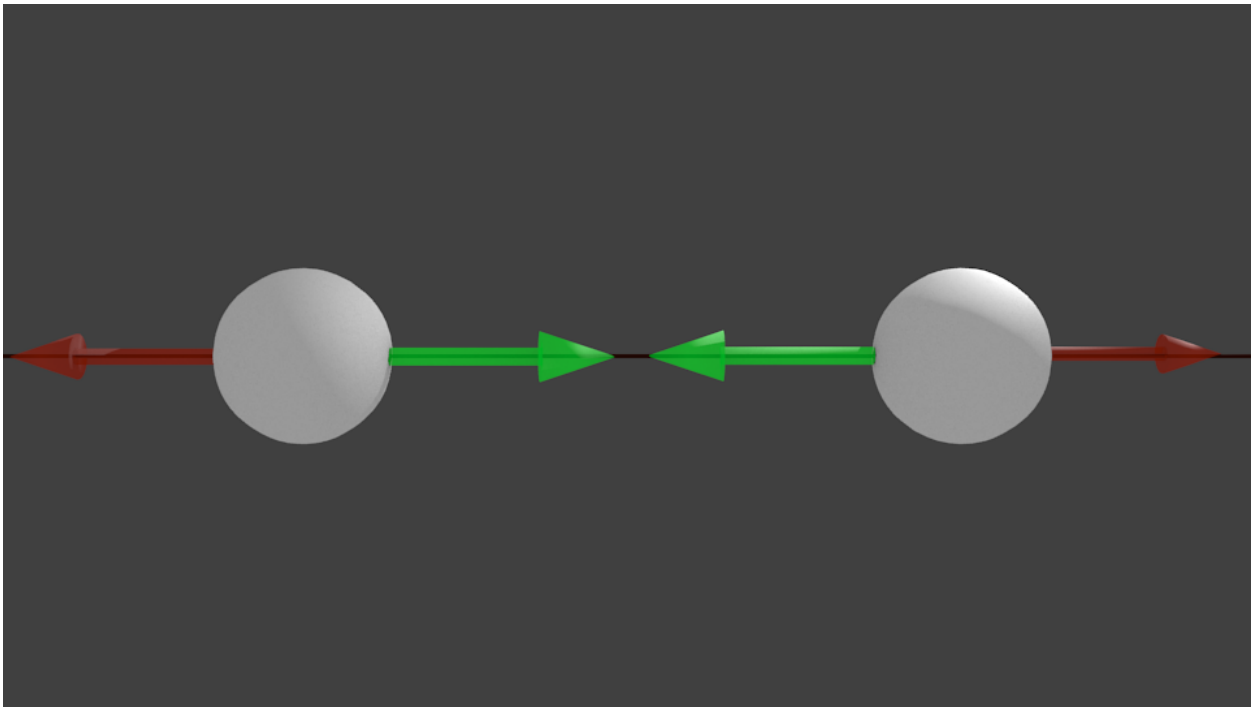

Figure S10: While the forces connecting the microtubule backbone must balance, these forces are a) axial and lack the symmetric cancellation of the quadrupole and b) the separation between them is the basis for the characteristic length scale of the microtubule itself, and is thus fixed in relation to the size scale of the interaction.

as we saw the kinesin forces fall off as $\mathbf{r}^{-3}$. This is not to say that the kinesin does not effect the system at all.

While the long range fluid motion will not be strongly influenced by the kinesin motor forces, these short range effects will allow the impellers and microtubule to move relative to each other. While the details of the local fluid motion are complex, the bulk effect is known; the kinesin walks along the microtubule at a steady rate, creating a fixed relationship between the impeller velocity and the microtubule velocity. Because the relative motion between the microtubule and the impeller layer is known, only the motion of the fluid at the impeller interface is needed to determine the motion of the system. As we have shown, the forces due to the kinesin motors directly do not contribute to the long range fluid motion, and the only remaining forces are those from microtubule backbone. Note that this does not contradict the analysis of Sec. 2 where we analyzed the hydrodynamics of a line of impellers. In both cases, the force on the fluid due to the power expenditure of the motors is the same. In the current analysis, we have separated out the internal force-pairs that were lumped together in the previous analysis. Instead of considering fluid flow to be directly caused by forces from the impeller as we did previously, we have considered all the separate elements, kinesin, impellers, tension, and microtubule curvature, that are all coupled to the fluid as expressed by Eq. S-30. What we showed above is that there is a cancellation of the long range fluid flow from the terms involving kinesin forces. The long range flow that remains is due to the tension and curvature terms. Because of Newton's third law, the long range flow in Sec. 2 is the same for these two descriptions.

This leads us to a method for determining the dynamics of the system. The Oseen tensor should be integrated over the force densities f_{int} along the backbone of the microtubule, ignoring the contribution from the impeller directly.

$$\mathbf{u}(\mathbf{r}) = \int_{backbone} \mathbf{f}_{int}(\mathbf{r}') \cdot \mathbf{J}(\mathbf{r} - \mathbf{r}') d\mathbf{r}' \tag{S-38}$$

This will give us the large scale fluid motion that will determine the large scale motion of the entire system. The coupling from the fluid back to the impeller/microtubule system will depend on the

short range fluid interactions brought about by the kinesin motors; however, we still expect the long range motion of the microtubule/impeller system to match that of the fluid. By symmetry, the difference in velocities will be axial, and the kinesin will still maintain a fixed relationship between the microtubule and impeller. From that we expect the fluid velocity to appear to be a weighted average of the microtubule and impeller velocity.

$$\mathbf{u}(\mathbf{r}) = \mathbf{v}_I(1-\delta) + \mathbf{v}_M\delta \tag{S-39}$$

Where $\mathbf{v}_I$ and $\mathbf{v}_M$ are the impeller and microtubule velocities, respectively. If we use the fact that $\mathbf{v}_I - \mathbf{v}_M = v_k\frac{\partial \mathbf{r}}{\partial s}$, we find an expression for our microtubule velocity

$$\frac{d\mathbf{r}}{dt} = \mathbf{v}_M = \mathbf{u}(\mathbf{r}) - (1-\delta)v_k\frac{\partial \mathbf{r}}{\partial s} \tag{S-40}$$

where v_k is the kinesin velocity. As we can see, the effect of the coupling on the microtubule motion is to act as though the kinesin velocity is suppressed by some fraction, relative to if the entire microtubule were covered with kinesin. This is the same result as was obtained in the single microtubule discussion (Sec. 2). While the exact value of this suppression depends on the detailed hydrodynamic interactions of the microtubule and impellers, the large scale behavior can be obtained by a simple rescaling of the walk speed, giving us the relation:

$$\frac{d\mathbf{r}}{dt} = \mathbf{u}(\mathbf{r}) - \mathbf{v}_k\frac{\partial \mathbf{r}}{\partial s} \tag{S-41}$$

5.4 Hydrodynamics near a hard wall

Up until now, we have only considered microtubules pinned at one end and unhindered by any other structures nearby. However our photobleaching tests (Fig. 7) and prior observations agree that microtubules are attached by their minus ends to the oocyte cortex. The presence of this stationary wall may have a significant effect on the microtubule motion, as it imposes a new boundary condition on the fluid motion; namely that the velocity must vanish at the wall.

This new boundary condition changes the Green's function used to construct the fluid velocity from the forces applied to the system. The determination of this Green's function is dependent on

the specific boundary geometry, and potentially intractable. Because of this, we will first investigate the case of an infinite plane hard wall at $z = 0$, to provide some insight into the behavior of the microtubule impeller system near the cortex.

Fortunately, the Green's function for the infinite wall case has already been solved[S10]. The technique is similar to that of the method of image charges in classical electromagnetism, with the added complication of the sources being vector quantities instead of scalers. This vector nature of the sources gives rise to a number of corrections to the simple reflection. It is somewhat complex, though not of higher order scaling than the unmodified Oseen tensor. The interaction $\mathbf{J}^w(\mathbf{x}, \mathbf{y})$ between a point force $\mathbf{f}$ at location $\mathbf{x}$ and a fluid location $\mathbf{y}$ is now:

$$\mathbf{J}^w(\mathbf{x}, \mathbf{y}) \cdot \mathbf{f} = \frac{1}{8\pi\mu\mathbf{r}^*}[-(\mathbf{I} + \frac{(\mathbf{r}^* \cdot \mathbf{f})\mathbf{r}^*}{\mathbf{r}^{*2}}) + \frac{2H}{\mathbf{r}^{*2}}((\frac{3x_3(\mathbf{r}^* \cdot \tilde{\mathbf{f}})}{\mathbf{r}^{*2}}\mathbf{r}^* - \tilde{\mathbf{f}}_3)\mathbf{r}^* - x_3\tilde{\mathbf{f}} + (\mathbf{r}^* \cdot \tilde{\mathbf{f}})\hat{\mathbf{z}})] \qquad \text{(S-42)}$$

Where $\mathbf{r}^*$ is equal to $(x_1 - y_1, x_2 - y_2, x_3 + y_3)$, the reflected displacement vector, $H = y_3$, the distance of the fluid from the wall, and $\tilde{\mathbf{f}} = (f_1, f_2, -f_3)$, the reflected force. One can recognize the first term as the reflected Oseen tensor, similar to a negative charge in the method of images. However, as previously mentioned, the fact that the force must also have its direction flipped adds several additional terms. These terms together ensure that the velocity of the fluid will vanish at the boundary.

Other than the modification of the interaction tensor, the model remains almost unchanged. Due to the assumptions used to generate this solution, it is of course only valid for $z > 0$, and can result in strange behaviors if applied for regions below the plane $z < 0$. These usually result in extremely singular velocities, and so care must be taken to ensure that no part of the finite time step used in a simulation will cross this boundary. To ensure this, a hard wall potential similar to that used for the hard core repulsion of the microtubule segments is placed at $z = 0$, as will be described in more detail below in Sec. 5.6.

5.5 Numeric Implementation of the Model

The complexity of the interaction makes analytic solutions difficult, however, the dependence of the fluid flow only on the current state of the microtubule makes it suitable for direct simulation. A straightforward integration of the velocity field will yield the complete system dynamics.

5.6 The discrete model

As with the single microtubule case, the microtubules are modeled as a chain of discrete points. The use of the long range fluid interactions prevents us from using pure rigid links, so this model uses a backbone comprised of stiff spring links, such that the force on each element is:

$$\mathbf{T}(\mathbf{r}_i) = k_T(|\mathbf{d}_{i-}| - l)\hat{\mathbf{d}_{i-}} + (|\mathbf{d}_{i+}| - l)\hat{\mathbf{d}_{i+}} \tag{S-43}$$

With

$$\begin{aligned} \mathbf{d}_{i-} &= \mathbf{r}_{i-1} - \mathbf{r}_i \\ \mathbf{d}_{i+} &= \mathbf{r}_{i+1} - \mathbf{r}_i \end{aligned}$$

Where $\mathbf{r}_i$ are the positions of the individual microtubule segments, with k_T being the backbone spring constant and l being the rest length of the segment. The spring constant is chosen to be as strong as possible for the given time step, in order to match as closely as possible to an incompressible chain. In addition to the spring force tension term, the backbone stiffness is modeled as a discrete fourth derivative along the spine, with an adjustable scaling parameter.

$$\mathbf{C}(\mathbf{r}_i) = -k_C[(\mathbf{r}_{i+2} - \mathbf{r}_i) - (\mathbf{r}_i - \mathbf{r}_{i-2})] \tag{S-44}$$

In order for the microtubules to not cross through each other, they are also given a hardcore repulsion force that is divergent at zero distance along with rapidly and smoothly falling off to zero at some characteristic radius d. This was implemented as a inverse fourth power law with a cutoff. In addition we also allowed for an attractive interaction between microtubules over a shell spanning

$d < r < d_a$, which we added as an explanation of the bundling of microtubules that is apparent in movies of fast streaming:

$$\mathbf{f_h}(\mathbf{\Delta r}) = \begin{cases} (1 - \frac{d^4}{\Delta r^4})\mathbf{\Delta r}, & \text{for } \Delta r < d \\ -\frac{32 * f_a}{(d_a - d)^2}(\Delta r - d)(\Delta r - d_a)(2\Delta r - d - d_a)\frac{\mathbf{\Delta r}}{\Delta r}, & \text{for } d < \Delta r < d_a \\ 0, & \text{for } \Delta r \geq d_a \end{cases} \tag{S-45}$$

$$\mathbf{f_H}(\mathbf{r}_i) = \sum_j \mathbf{f_h}(\mathbf{r}_i - \mathbf{r}_j) \tag{S-46}$$

The attractive force is normalized so that the minimum depth of the corresponding potential is $-f_a$.

In addition to the bulk forces, there are also boundary cases, as well as tethering the minus-ends of the microtubule. The tethering is accomplished simply by including a spring force, similar to the tension spring force, that is centered to a specific fixed point in space. All of these forces are directly transmitted to the fluid, and thus must be included in the Oseen tensor calculation. There is a difficulty when transitioning to the discrete case due to the singularity of the Oseen tensor at the origin. For this reason, the effect of the forces generated on a specific segment on the fluid at the same location is more difficult to determine. The standard practice in this case is to use the Oseen tensor as an interaction between elements, and to use a simple free draining drag model for the local motion. Since our microtubule is modeled as a long chain of beads we simply use the drag due to a small sphere

$$\mathbf{J}_{ii} = \frac{1}{4\pi\mu}. \tag{S-47}$$

By combining equations S-43, S-45, S-44, and S-38, we see that for any point in space, the fluid velocity is given by:

$$\mathbf{u}(\mathbf{r}_i) = \mathbf{J}_{ii}[T(\mathbf{r}_i) + C(\mathbf{r}_i) + H(\mathbf{r}_i)] + \sum_{j \neq i} \mathbf{J}(r_i - r_j)[\mathbf{T}(\mathbf{r}_j) + \mathbf{C}(\mathbf{r}_j) + \mathbf{f_H}(\mathbf{r}_j)] \tag{S-48}$$

However, due to the relative velocity between the fluid and the microtubule backbone, the velocity used to update the position of the microtubule locations r_i is found by subtracting the kinesin walk speed.

$$\frac{d\mathbf{r}_i}{dt} = \mathbf{u}(\mathbf{r_i}) - \frac{\mathbf{1}}{\mathbf{2}}\mathbf{v_k}(\mathbf{r_{i-1}} - \mathbf{r_{i+1}}) \tag{S-49}$$

This derivative is then used for a standard fourth order Runge Kutte integration in order to advance the system in time.

5.7 Single Microtubule verification

The new algorithm was then used to simulate a single microtubule in order to see what effect the fluid interaction would have on the single microtubule solution. Because this simulation does not apply any external flow fields, we expect the solution to closely resemble the zero field case from the theory without fluid coupling (see Sec. 4).

We ran this simulation using the same parameters for a single microtubule with and without the fluid interaction, again using a random starting configuration and tethering the minus-end of the microtubule to a fixed point in space. The result was essentially as expected, with a solution that asymptotically approached a circle rotating at a constant rate (Fig. S11).

It is interesting to note that the hydrodynamic interaction has little to no effect on this type of solution.

5.8 Properties of the Many Polymer Model

More microtubules are added to the simulation, so that there are on the order of tens to hundreds of them. The microtubules have their minus ends tethered in a planar configuration, to mimic tethering to the cortex. Spacing between the individual anchors can be varied, but will never be close enough for their hardcore radii to overlap.

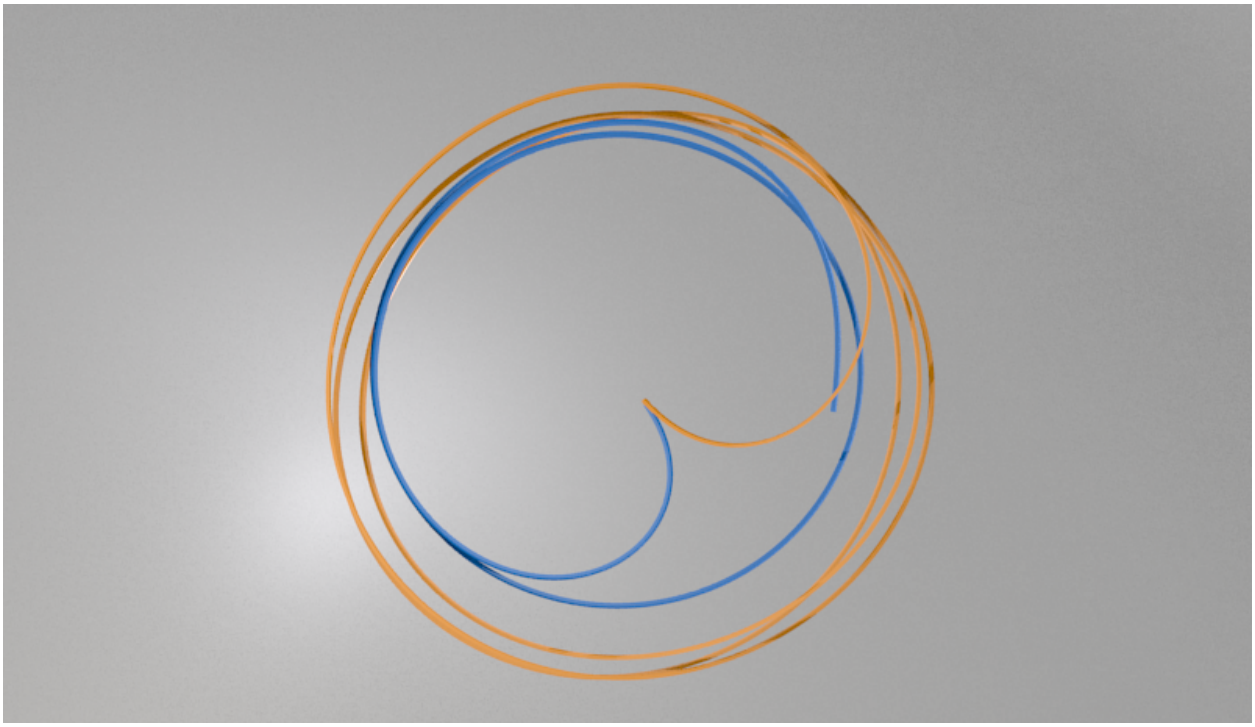

Figure S11: Simulation results for a single polymer without fluid interaction(blue) and with fluid interaction(orange), with all other parameters held the same. Both polymers are tethered at the center of the image, near the center of the circular configuration. The images are super imposed, but the polymers were simulated separately. They are qualitatively the same, though the radius is slightly larger with fluid interactions activated.

5.9 Important Length Scales

The introduction of more than one microtubule, along with the addition of the hard wall, introduces new length scales to the system. The microtubules are placed with their tether points in a plane parallel to the hard wall, each initialized with a random configuration subject to the constraint that they not pass through the wall. Within this plane, the tethered minus ends have a characteristic separation, R_s, and this separation defines one of the new length scales in the system.

In the oocyte, the hard wall is the plasma membrane and a closely associated dense meshwork of proteins, including filamentaous actin. Inward from that, the f-actin meshwork becomes less dense. The inward side of this cortical meshwork is loose enough to allow fluid flow, but able to tether microtubules such that their initial point of bending (tether point) is at some distance away from the impenetrable oocyte wall. For this reason we study microtubule patches that are at some small fixed distance H away from the hard wall boundary. Although the real situation involves a more complicated flow, due to the meshwork described above, we expect that this should be similar to our system with H chosen appropriately. In addition, the means by which they are attached may hinder rotation about the attachment, so if they are pointing perpendicular to the oocyte wall, then they will be effectively raised from it. For these reasons, we take the separation between the plane of the hard wall and the plane of anchors, H, to be nonzero. This represents a second new length scale.

These two new lengths are set to be less than the characteristic buckling length of the microtubule, R_b, in order to more closely match what is seen in the biological data. We will see that these two length scales play an important role in determining the correlation behavior of the system.

5.10 Correlation Between Multiple Microtubules

A key feature found during fast streaming is the formation of correlated groups to enable larger scale coordinated forces on the fluid. These correlations arise as the motion of fluid near a microtubule causes that microtubule to align with the preexisting flow. The microtubules contribute to that

flow because a type of field amplification occurs. Essentially, the long range interaction through the cytoplasmic fluid could bring about a transition to a phase of long range order.

When the simulation is run with a small number of microtubules placed with their tethered minus-ends near each other (less than the microtubule buckling length), short range correlation almost always emerges. Using a random walk starting condition, the microtubules initially fall into seemingly independent circular solutions similar to those of the single microtubule case. However, after a few periods of revolution the microtubules eventually collapse into one circular solution (see Fig. S12).

While this correlation is a promising feature, it is not enough to produce a long range directed flow field, particularly because of the circular nature of the motion. To sustain linear streaming, the forces transmitted to any one microtubule from the rest of the system need to be stronger than the local kickback force from the kinesin motors. A small number of microtubules will not be able to achieve this.

5.11 Microtubule Patches

To attain linear streaming in our simulation, we include more microtubules. These microtubules are placed with their minus-end anchor points in a square grid, and then some small random jitter is applied within the plane to their positions. The random noise is added to suppress periodic lattice effects, which should not be present in the cell. Once the anchor points are chosen, the microtubules are initialized with a random walk biased slightly in the positive z direction to avoid problems caused by starting in the hard wall. Any configuration that penetrates the wall is rejected. Due to the random nature of the initial conditions, the microtubules often start with high curvatures. This causes the first few steps of the simulation to be dominated by the microtubules rapidly relaxing to their more typical curvature. This artifact of the somewhat artificial initial conditions should not be relevant to the actual biological system, so these initial steps are not shown. The forces that cause this relaxation are quite high, and occasionally they can cause the microtubules

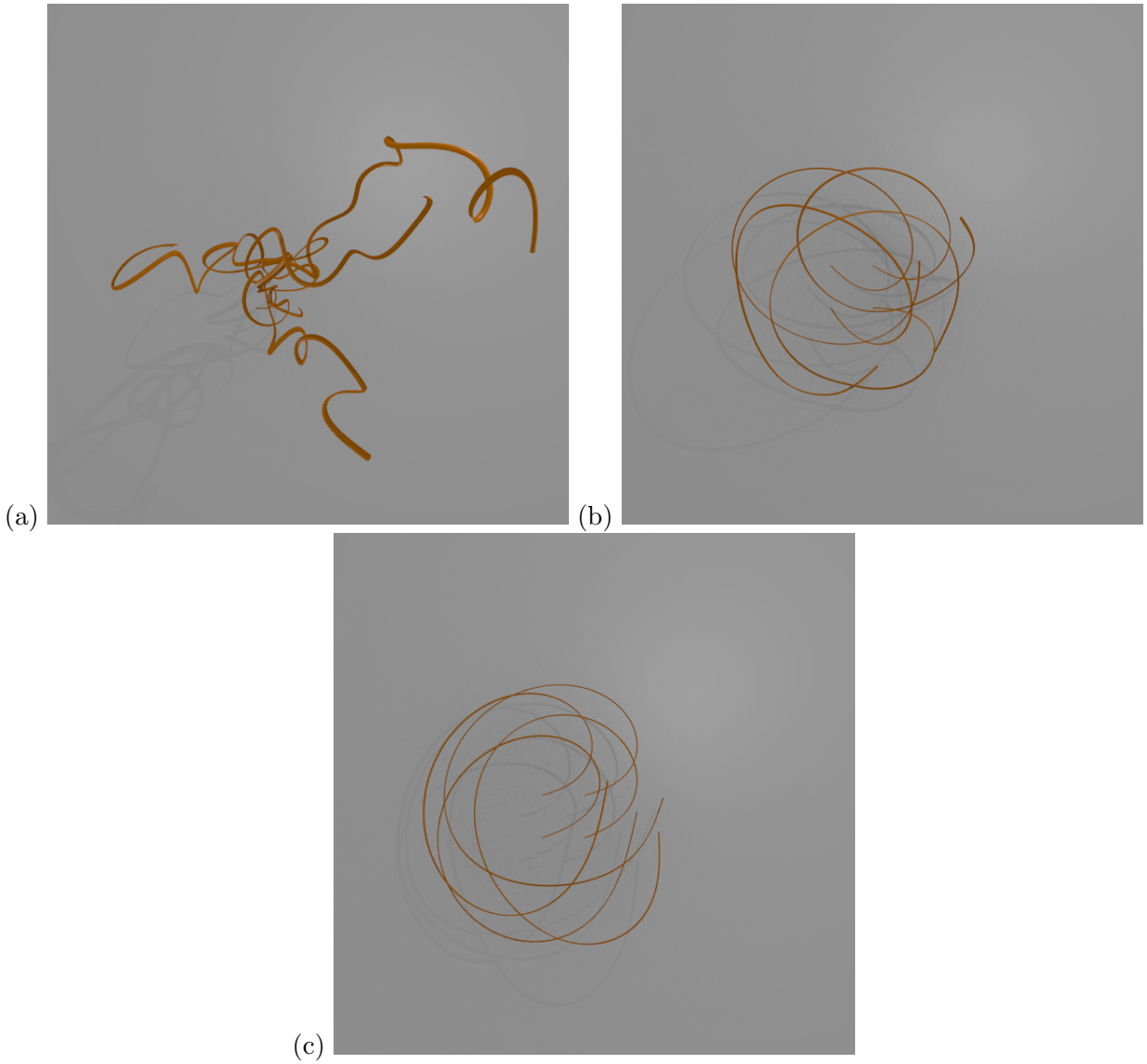

Figure S12: (a) A typical starting configuration of four microtubules, with $R_s = 2$ and $H = 2$. The apparent thickness is an artifact of the display method. (b) After a short time, the microtubules fall into individual circular solutions, with some correlation. (c) After a few revolutions, all of the microtubules collapse into correlated circles.

to break through the hard wall. This most often results in a divergence due to the hard wall Oseen tensor having odd behavior for negative z values. Initial conditions that lead to this effect are also rejected. A typical initialized patch is shown in Fig. S13 To check that these extreme initial conditions were not influencing our final steady state behavior, and to improve the realism of the model, we employed a Monte Carlo algorithm to initially anneal the chains to give more realistic curvatures. This greatly improved the robustness of our initial configurations preventing the breakthroughs mentioned above. However, it had no discernable effect on the steady state behavior despite testing the simulation with a wide variety of different conformations.

5.12 Linear Streaming with Microtubule Patches

There is a fairly wide range of parameters for which, regardless of the random initialization, the microtubule patch will self organize into a stable directed flow (Fig. S14).

The length of time needed for the patch to reach this linear streaming phase can vary based on the parameters of the simulation, but in general it will be within a few periods of the single microtubule rotation. During this correlation time, smaller sub regions of extended microtubules appear. These sub regions can slowly rotate as a unit, and tend to cause more microtubules to correlate along with them as they pass nearby. Once established, the linear streaming regions are stable and settle into a single direction.

It is important to re-emphasize that there is no externally imposed fluid motion in this simulation, and that the linear configuration is brought about by fluid mediated interactions between microtubules. The final direction of the array and of streaming is dependent on the exact nature of the random initial conditions, which are not guaranteed to be perfectly isotropic. The spontaneous generation of this ordered phase will cause some aspects of the resulting system, such as the direction of the resulting global flow field, to depend sensitively on the initial conditions of the system. However, many properties of the system in this phase, such as the flow speed and characteristic oscillation frequencies, should be independent of the initial conditions. As long as the microtubules

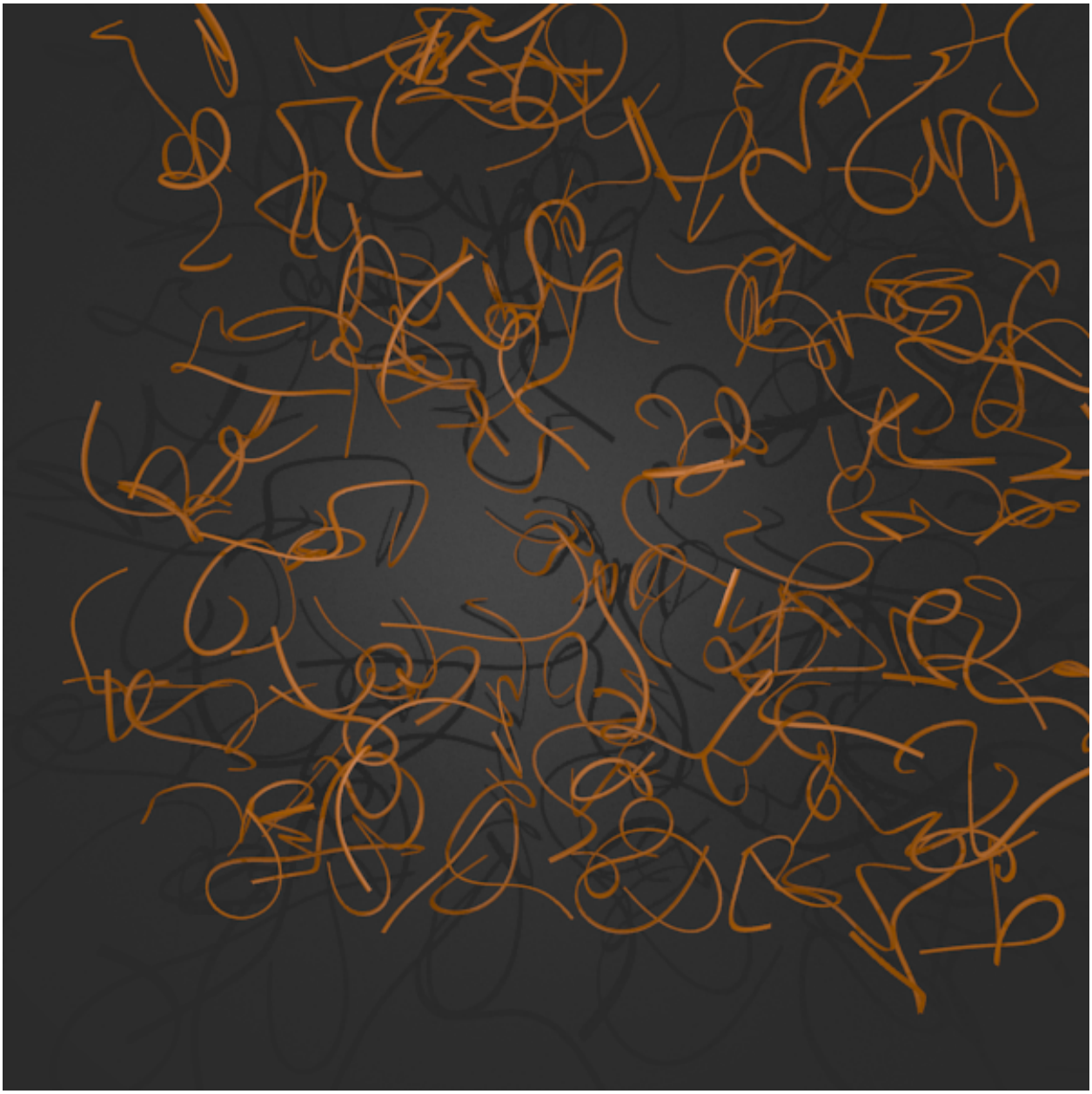

Figure S13: A typical starting configuration for a microtubule patch, viewed from directly above the plane of the hard wall. The microtubules are tethered at their minus ends in a square grid pattern above the wall by the same distance as the separation between the anchor points. The grid of anchor points occupies the majority of the view, though it is slightly shifted to give a better view of the microtubules.

Figure S14: A typical configuration after correlation, viewed from an angle to better show the planar nature of the solution. The grid of anchor points is significantly farther from the hard wall boundary in this simulation than was used in the previous image, in order to increase long-range correlation. The microtubules minus-ends are tethered at their rightmost endpoint in this image, and the fluid flow is left and upward, away from the viewer. The microtubules on the edges of the patch can be seen to execute a helical pattern reminiscent of the single microtubule dynamics.

are essentially at rest in a steady state, the fluid velocity should be determined by the analysis in Sec. 2.

5.13 Disordered Solutions

For some ranges of input parameters, the system does not align well enough to create the fast linear streaming phase. When the fluid interaction forces are not sufficient to overcome the kinesin reaction force, individual microtubules buckle and begin rotating around their tether points. Even though the hydrodynamic interaction is not strong enough to force a straight line solution, it can still cause the rotational solutions to correlate with each other, much like in the case of just a few microtubules (see Sec. 5.10 above). Regions of correlated microtubules can develop (Fig. S15). The dynamic correlations found in this phase might include large numbers of microtubules, but rarely include the anchor points. These masses of loose microtubule ends tend to flow back along their length, and as such generate very little long range fluid motion.

5.14 Conditions for Linear Streaming

Not all microtubule patches will reach the linear streaming phase from a random initial condition. There are ranges of parameters for which the system will only exhibit short range correlation, often in the same manner as the systems with only a few microtubules. In these cases the forces from the fluid interaction are not strong enough to overcome the local kinesin reaction force, and the microtubules buckle and rotate around their anchor points.

Whether a system will reach the correlated directed fast streaming phase is determined by a number of parameters that effect the relative strength of the forces in the system. These parameters can be the internal properties of the microtubule/impeller system, or properties of the arrangement of the microtubules in the patch.

In the next section we will investigate the effects of a wall on the system's propensity for linear streaming and show that it plays an important role.

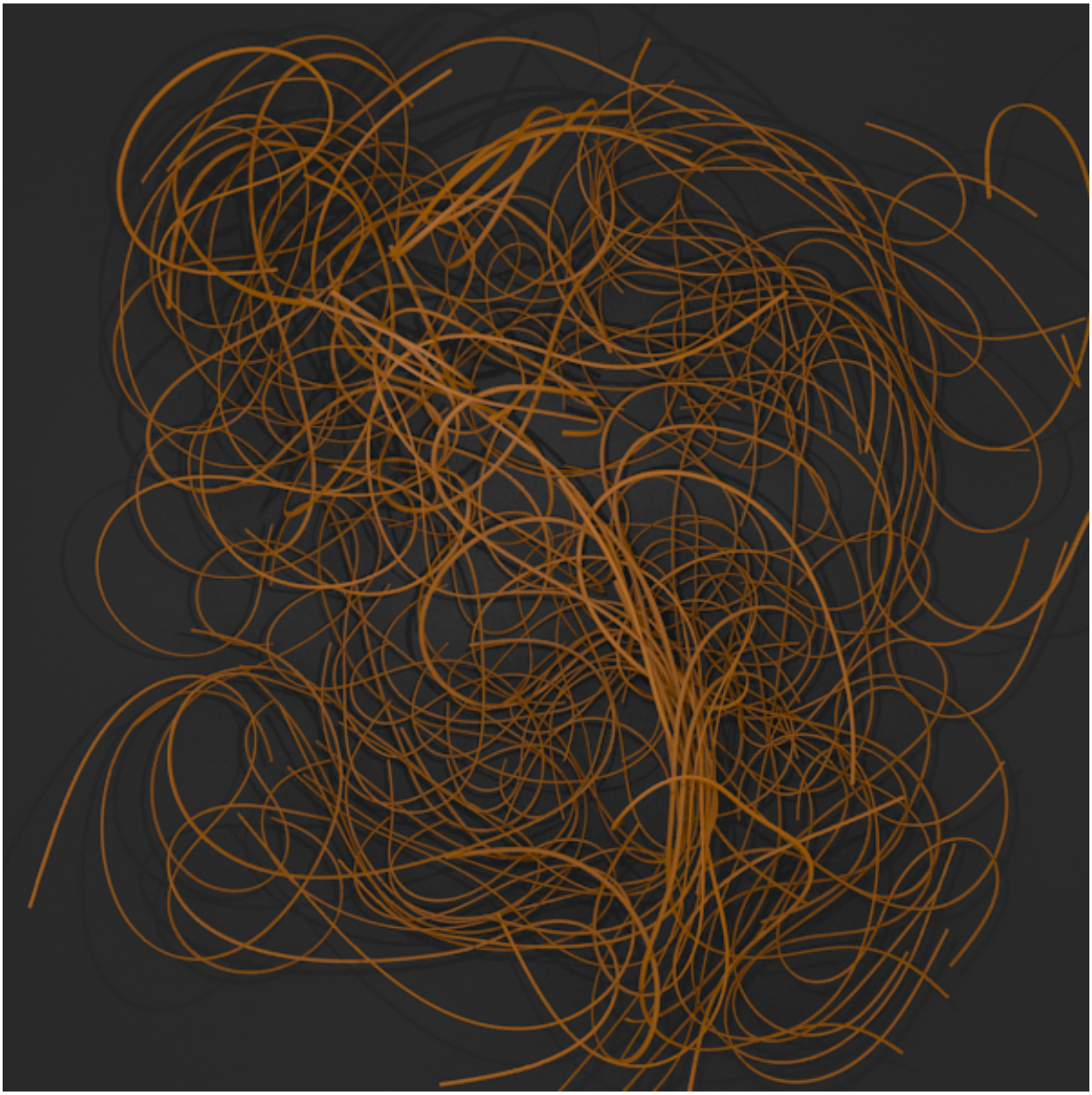

Figure S15: A system that does not achieve directed fast streaming. It does show temporary local correlations, but these are not stable in any one direction.

5.15 Effects of the wall

The hard wall serves to damp out fluid motion near its surface due to its strong interaction with the fluid viscosity. This is seen in the interaction tensor as a negative force mirrored across the wall, opposing the motion of the true force above it. One can imagine that, much like the case in electromagnetism, these mirror forces could form some sort of dipolar arrangement. This arrangement would have faster falloff with distance and could easily interfere with the ability of the entire system of microtubules to correlate over large distances. We can see this effect in the simulation by simply placing the microtubule patch at several distances from the wall while holding the other parameters fixed (Fig. S16).

At large elevations above the wall, the patches reach the linear streaming phase from the random initial state quite rapidly(within only a few rotation periods). As the elevation is decreased, the time the system takes to reach the linear streaming state increases.

Eventually, the wall decreases the interaction strength significantly enough that the nucleation of the linear streaming regions cannot occur. At these distances, the microtubules will often still correlate, but do not manage to achieve the straight line configuration.

5.16 Relative Viscosity

One can also vary the viscosity of the fluid in this system. As can be seen from Eq. S-48 and S-29, there is a global factor of μ^{-1} on all of the driving force terms. Changing the viscosity on any given system will then inversely effect the fluid velocity field from any given set of forces. At first, it might seem that this would only cause a change in the overall timescale of the dynamics, but that turns out to be incorrect. The motion of the microtubule itself is given by Eq. S-49, which includes a term only proportional to the kinesin walk speed. If this speed remains unchanged, the effect of the kinesin forces will be scaled proportionately to the viscosity.

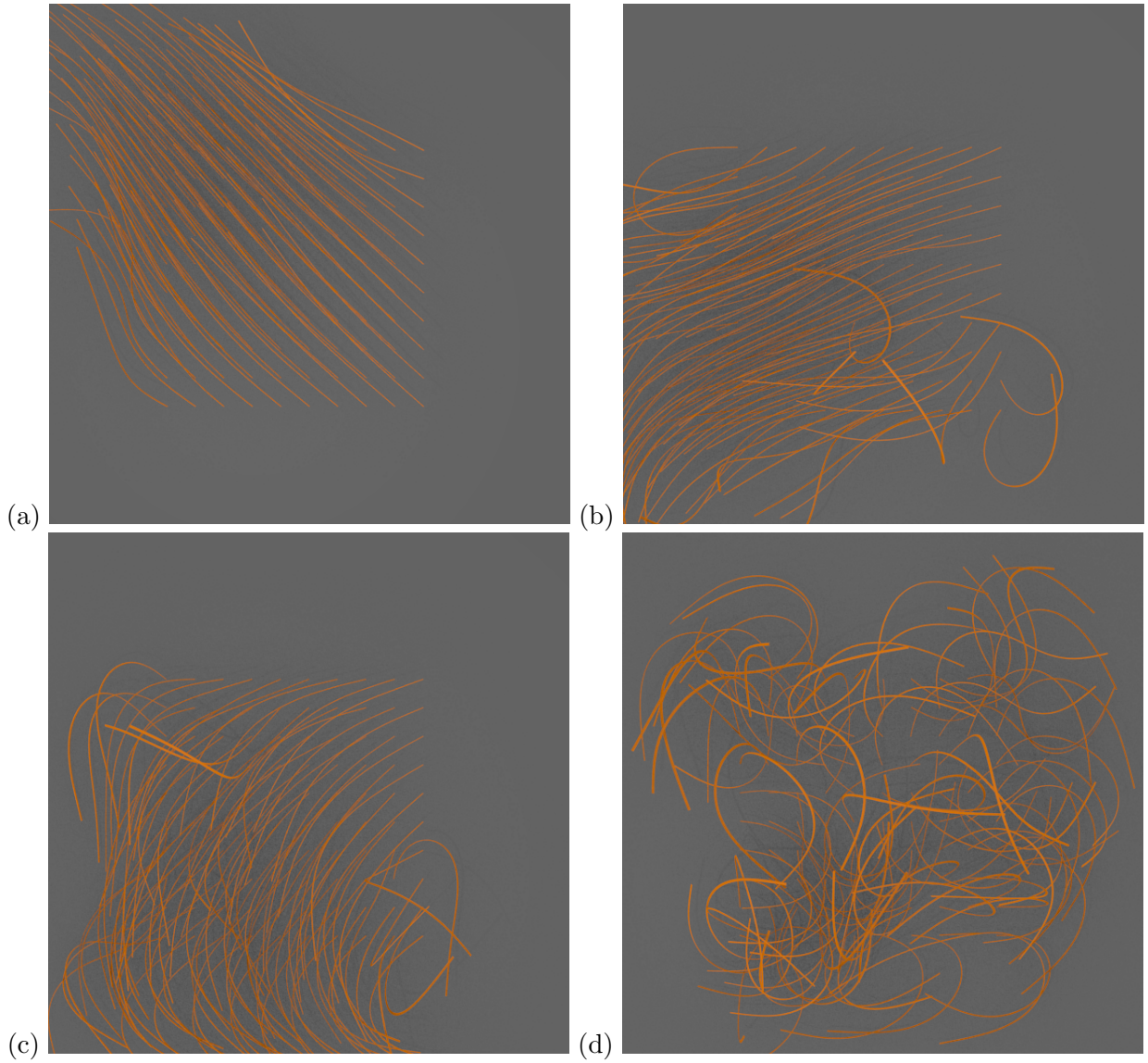

Figure S16: (a-d) Configuration of microtubule patches after 200 simulation frames. (a)Patch at $H = 5$, shows strong directed streaming (b)Patch at $H = 3$, shows directed streaming, but with more loose edges (c)Patch at $H = 2$, shows directed streaming, but propagates large correlated "waves" and is not as straight (d)Patch at $H = 1$, shows no directed streaming, only short range correlated circular motion.

5.17 Hysteresis of Streaming

Because it is a self reinforcing effect, the fast streaming behavior could very easily depend on the initial configuration of the microtubules. For instance, it is believable that a system could be just barely able to support streaming with the microtubules aligned, but that such a system would be unable to spontaneously generate that alignment. This divides our phase space up into additional regions. One region is where the system always transitions to correlated streaming. One would imagine that this region would be one where interactions between microtubules are strong and long range compared to the other length scales in the system. Another region is one where the system can support fast, correlated streaming, but may only reach it from certain classes of initial configurations. This region is obviously less robust if the intent is to achieve fast streaming. A third region is one in which the system can never support fast correlated streaming. This would most likely be a region in which the interaction between microtubules is cut off at a range less than the typical spacing between microtubules.

We focus here primarily on the transition from disordered microtubules into correlated fast streaming. This focus comes from the behavior of the cell during the stages before and after the start of fast streaming. In the oocyte, microtubules are observed to be largely non-correlated or correlated in circular motions during the slow streaming phase (Movie S1), while they are observed in strongly correlated arrays during fast streaming (Movies S2 and S3). The oocyte likely undergoes changes in key streaming parameters to cross the phase boundary from weakly correlated slow steaming to strongly correlated fast streaming. It is well known that reductions in cytoplasmic f-actin and an inward shift of microtubule minus ends coincide with the shift from slow to fast streaming [8,15,16,36].

Supporting References

[S1] Meyhöfer, E. and Howard, J. (1995). "The force generated by a single kinesin molecule against an elastic load." Proc. Natl. Acad Sci. USA. **92** 574-578.

[S2] Yin, H. L. and Stossel, T. P. (1979). "Control of cytoplasmic actin gelsol transformation by gelsolin, a calcium-dependent regulatory protein." Nature **281**, 583-586.

[S3] Cushman, R. H. and Bates, L. M. (1997). "Global aspects of classical integrable systems." Birkhäuser (Basel, Boston, Berlin), Ch. IV.

[S4] Kessler, D. A., Koplik, J., and Levine H. (1985). "Geometrical models of interface evolution. III. Theory of dendritic growth." Phys. Rev. A **31** 1712-1717.

[S5] Barbieri, A., Hong, D. C., Langer, J. S. (1987). "Velocity selection in the symmetrical model of dendritic crystal growth." Phys. Rev. A **35** 1802-1808.

[S6] Deutsch, J. M. (1988). "Theoretical Studies of DNA During Gel electrophoresis." Science **240** 922-924.

[S7] Deutsch, J. M. and Madden, T. M. (1989)."Theoretical Studies of DNA During Gel electrophoresis." J Chem. Phys. **90** 2476-2485.

[S8] Deutsch, J. M. (2010). "Internal dissipation of a polymer." Phys. Rev. E **81**, 061804/(1–6).

[S9] Landau, L. D. and Lifshitz, E. M. (1970). Theory of Elasticity, 2nd ed., Pergamon Press.

[S10] Dabros, T. and van de Ven, T. G. M. (1992). "Hydrodynamic Interactions Between Two Spheres Near a Solid Plane." Int. J. Multiphase Flow **18**, 751-764.